SEARCHES FOR VECTOR-LIKE QUARKS WITH THE ATLAS DETECTOR AND DESIGN OF THE TYPE-0 SERVICES FOR THE ITK UPGRADE

By

EVAN VAN DE WALL

Bachelor of Science in Physics
Ithaca College
Ithaca, NY
2016

Submitted to the Faculty of the
Graduate College of the
Oklahoma State University
in partial fulfillment of
the requirements for
the Degree of
DOCTOR OF PHILOSOPHY
August, 2023

SEARCHES FOR VECTOR-LIKE QUARKS WITH THE ATLAS DETECTOR AND DESIGN OF THE TYPE-0 SERVICES FOR THE ITK UPGRADE

Dissertation Approved:

Dr. Joseph Haley

Dissertation Advisor

Dr. Flera Rizatdinova

Dr. Mario Borunda

Dr. J. Cecil

ACKNOWLEDGMENTS

I took my first physics course in my senior year of high school and hated it. I mainly was looking at engineering programs for undergrad and applied to the Math department at Ithaca College. While deciding which school to attend, I met with Dr. Bodhi Rogers of the Ithaca College physics department and understood nothing said. It is wild to think that I have my doctorate in physics because this one professor in a department I didn't apply to took some time to meet me.

I cannot express my gratitude enough to the staff and faculty of the Ithaca Physics Department. They showed me the joy of learning physics and the excitement of doing research. Bodhi not only met with me that day, but he also became my research advisor, and his mentoring showed me that I could be where I am today.

Like undergrad, I attended Oklahoma State because a professor took some time to meet with me when deciding where to go to grad school. Dr. Joe Haley saw my application and reached out to me, and I met with a professor in a field I knew nothing about. Joe made me feel welcome, and his mentorship is a big reason why I am here.

I also want to share my thanks to the other professors of the OSU HEP team. They are some of the kindest and most helpful people one could wish to study under. I also want to thank Steven for his mentorship in the engineering side of HEP. The experience I gained from him has put me in a position I would not have imagined possible.

While I can never express enough gratitude for the staff and faculty that taught me

Acknowledgments reflect the views of the author and are not endorsed by committee members or Oklahoma State University.

and trained me, another big group of people helped me succeed. The friends I made through my career have been unbelievable. Not only at the universities I attended but honestly all over the world. Every person and group I have met and interacted with has been unique and unforgettable, but one group deserves more thanks than the rest. My friend group back home in Waverly is my rock. I know that I had them there to call no matter what happened.

This last year I was lucky enough to have my wonderful girlfriend, Fer, next to me. Things haven't all been easy, but she helped me stay calm throughout this challenging time.

The final people who I would like to thank are my family. They have supported me through this whole process. Their love and support were something I knew I could count on. I knew I always had them in my corner when things were feeling rough.

Thank you to everyone!

Name: EVAN VAN DE WALL

Date of Degree: AUGUST 2023

Title of Study: SEARCHES FOR VECTOR-LIKE QUARKS WITH THE ATLAS DETECTOR AND DESIGN OF THE TYPE-0 SERVICES FOR THE ITK UPGRADE

Major Field: PHYSICS

Abstract: The Standard Model (SM) of Particle Physics has enjoyed unprecedented success in describing the universe at the subatomic level. Yet, it must not be a complete theory of nature as it does not include gravity, cannot explain dark matter, provides no insight into huge hierarchies in forces and masses, and so on. Many extensions to the SM aimed at addressing these shortcomings predict the existence of a new type of particle called vector-like quarks (VLQs). This thesis presents the latest status of two searches for VLQs using the full Run 2 data set of 13 TeV pp collisions produced by the LHC and recorded by the ATLAS detector. The main focus will be on a new search for the pair-production of VLQs that each decay into a light SM quark and W boson. The second search targets top-partner VLQs produced in pairs, each VLQ then decaying to a W boson and b-quark. These represent the latest status of searches for VLQs with charged current decays with the current ATLAS detector. Looking to the future, the ATLAS detector will soon undergo an extensive upgrade in preparation for the High-Luminosity LHC, including installing a completely new, all-silicone tracking system called the Inner Tracker (ITk). This thesis highlights the development and design of the Type-0 electrical services for the all-new ITk Pixel tracking system that will lie at the heart of the upgraded ATLAS detector.

TABLE OF CONTENTS

LIST OF TABLES

LIST OF FIGURES

CHAPTER I

Introduction

1.1 Standard Model of Particle Physics

The Standard Model of particle physics (SM) is the theory that combines quantum mechanics and special relativity to describe the known fundamental particles and how they interact (except for gravity). There are two groups of particles within the SM, fermions, and bosons. Fermions are particles that have a half-integer spin and makeup matter. Gauge bosons have an integer spin and mediate the forces between the fermions. The Higgs boson is the final piece of the SM discovered in 2012, giving mass to all the fundamental particles [6, 23]. Figure 1 shows all the particles in the SM. While the SM has many successes, the SM does not have answers for many phenomena in the Universe, indicating that the SM is incomplete. Many analyses, including those discussed in this thesis, search for new particles beyond the SM to address these questions.

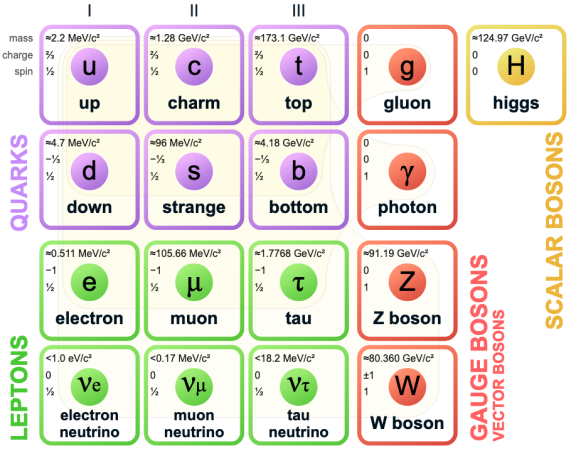

Figure 1: Diagram showing all the particles in the standard model of particle physics [40].

1.1.1 Fermions

Leptons and quarks make up the fermions of the SM. Leptons and quarks both interact via the electromagnetic force and the weak force. The primary difference between leptons and quarks is that quarks have color charge allowing them to interact via the strong force. These particles are then further divided into three generations. Each

generation is the same, except the mass of the particles increases with the generations. The particles of the higher generation will quickly decay to the particles of the first generation making the matter of the Universe consist of only particles of the first generation.

Both leptons and quarks have an electric charge allowing them to participate in Electromagnetic interactions, but the charge of each particle differ by their magnitude. Leptons have an integer charge, while quarks have a fractional electric charge. Electrons, muons, and taus have an electric charge of negative one, and neutrinos are neutral. The up-type quarks (up, charm, top) have a charge of +2/3, while the down-type quarks (down, strange, bottom) have a charge of -1/3.

Under the gauge symmetries of the SM, fermions are either left or right-handed. Left-handed fermions are arranged in weak isospin doublets, while the right-handed fermions are in weak isospin singlets. This property makes it so only the left-handed fermions can participate in the charged weak interaction, changing one particle in the doublet to the other. For example, the electron will switch to the electron neutrino under a weak charged interaction. The electroweak currents of the SM have a $V - A$ structure ($\bar{q}\gamma^{\mu}\left(1-\gamma^{5}\right)q'$) because the left-handed projector. SM fermions are chiral since only the left-handed particles participate in the charged weak interaction.

Quarks are the only SM fermions that interact via the strong force. Due to the color charge of the particles, they are unable to exist in nature independently. This property is called confinement. Quarks can only exist in groups of two or three, called hadrons, if the resulting color of the hadron is neutral (black or white). If the quarks are in groups of two, there must be a quark and an anti-quark group together such that the color of the quarks cancel, such as green and anti-green. These quark anti-quark pairs are called mesons. A group of three quarks is called a baryon. Each quark in the baryon must have a different color.

1.1.2 Gauge Bosons

Gauge bosons are particles in the SM with a spin value of one and mediate the forces between the fermions. These particles are photons, W bosons, Z boson, and gluons. Photons mediate the electromagnetic force. They interact with particles with electric charge, causing like charges to repel and opposite charges to attract. The W and Z bosons mediate the weak force. The Z boson is neutral, while there are two W bosons, one with a positive charge and one with a negative charge. Gluons mediate the strong force. They have no electric charge but have color charge. Each gluon has one color charge and one anti-color charge. There are a total of eight different gluons in the SM.

1.1.3 Higgs Boson

The final particle of the SM is the Higgs boson. The ATLAS and CMS collaborations at CERN discovered this particle in 2012. This particle is a scalar, meaning that the particle's spin is zero. All particles in the SM obtain a mass by interacting with the Higgs boson. A massless particle, such as the photon, does not directly interact with the Higgs boson.

1.2 Standard Model Limitations

With all the SM's success, some problems remain unanswered, showing that the SM is incomplete. A few of the shortcomings of the SM is the matter/anti-matter asymmetry in the Universe, the existence of dark matter, and the observed mass of the Higgs boson. Many extensions to the SM have been proposed, such as Supersymmetry, to answer these shortcomings. The analyses discussed in this thesis search for particles that address the observed mass of the Higgs boson (hierarchy problem).

1.2.1 Hierarchy Problem

The hierarchy problem is related to the observed mass of the Higgs boson being 17 orders of magnitude different than the calculated mass [17]. The calculation for the mass of the Higgs boson is $M^2_{\text{Higgs}} = \mu^2 + \delta^2$, where μ is the true mass of the Higgs boson and δ is a quantum correction term from interactions with other particles, like that shown in Figure 2.

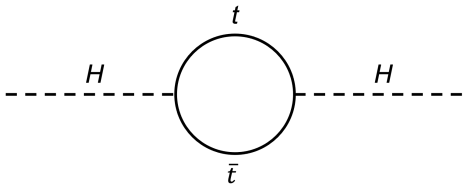

Figure 2: Feynman diagram of an interaction which adds to the quantum correction term in the calculation of mass of the Higgs boson.

The value of μ is the mass of the Higgs boson if it existed in a vacuum without interacting with any other particles and cannot be measured. The value of δ can be calculated using Feynman calculus and diverges to the Plank scale (10^{19}). For the mass of the Higgs to be 125 GeV, the first 32 digits of μ^2 must be the same as δ^2, unless there is new physics beyond the SM to cancel divergent contributions from the top quark. With vector-like quarks, new interactions with the Higgs boson are introduced, such as shown in Figure 3, which reduces the value of δ and solves the hierarchy problem.

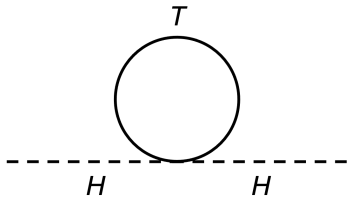

Figure 3: Feynman diagram of an interaction between a VLQ and Higgs boson which helps to reduce the quantum correction term in the Higgs boson mass calculation.

1.3 Vector-like Quarks

Theorists have introduced many theories to answer the questions not solved by the SM. Many of these theories address the hierarchy problem, such as Little Higgs and Composite Higgs include vector-like quarks (VLQ) [16, 31]. These particles introduce new interactions with the SM Higgs boson, which reduces the δ term in the mass calculation.

VLQs are particles that have both color charge and fractional electric charge like SM quarks. Unlike the SM quarks, the left and right-handed VLQs behave the same in the charged weak interaction, resulting in a vector electroweak current $\left(\bar{Q}\gamma^{\mu}Q'\right)$. A consequence of this vector current is that VLQs do not require coupling to the SM Higgs boson to obtain a mass. This is important since current measurements of the production rate of the Higgs boson exclude the existence of a fourth generation of chiral quarks [7, 33].

VLQs can be produced in pairs or singularly. Figure 4 shows the Feynman diagrams for both single and pair production of VLQs. Pair production of VLQs is via a strong force interaction, so only the mass of the VLQ matters when calculating the production rate (cross-section). Single production of VLQs happens via an electroweak interaction. The cross-section for this type of interaction depends on both the coupling strength and the VLQ's mass. While two parameters need to be scanned for single production, as the mass of the VLQ increases, the production rate of single production will overcome the rate of pair production. Figure 5 shows the cross-section as a function of mass for both single and pair production of VLQs. The colored lines show the cross-section for single production with the maximum allowed coupling. The dotted line shows the cross-section for pair production

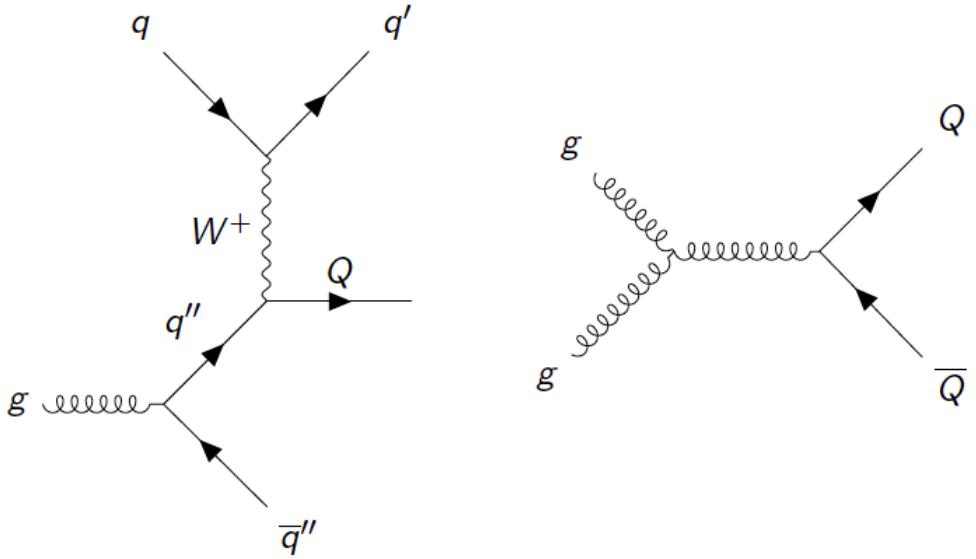

Figure 4: Feynman diagrams of single production (left) and pair production (right) of vector-like quarks (Q). Single production is created from an weak force interaction while pair production is created from a strong force interaction.

In the models of interest, VLQs can decay to SM quarks via the W, Z, or Higgs

boson since there is some mixing between SM quarks and VLQs. The decay process of VLQs is model dependent. In models such as the composite Higgs model, the lightest VLQ couples almost exclusively to the third generation of quarks [31]. This preferential coupling to third-generation quarks gives the VLQ the name "top partner." Some models do have the VLQs decaying primarily to light quarks (up, down, strange, or charm) [22, 31, 39]. Many searches within the ATLAS collaboration have focused on the "top partner" [1, 3, 4, 5], leaving searches for VLQ decaying to light quarks largely ignored [8].

Phenomenologically, the main difference between the different models of VLQs is the branching ratio to the three SM bosons. With so many models to check, the branching ratios are studied instead of independent models. The last step in the searches for VLQs is to check the sensitivity to all branching ratios.

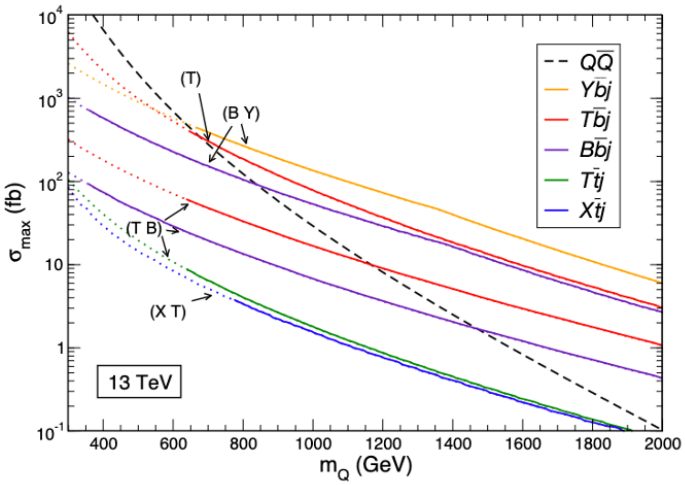

Figure 5: Plot showing the cross-sections for pair production of VLQs in the dotted line and single production of VLQs in different models with the maximum coupling in the colored lines [13].

CHAPTER II

The Large Hadron Collider and the ATLAS Detector

Studying parameters of the SM, or searching for the existence of new particles, requires energy levels close to that of the big bang. The Large Hadron Collider (LHC) can achieve energies previously unreachable to study these physical phenomena. This chapter discusses the LHC and the multi-purpose detector used in this research.

2.1 The Large Hadron Collider

The LHC [20] is a 27 km long particle accelerator operated by the European Organization for Nuclear Research (CERN), which spans the border of France and Switzerland 100 m underground. This accelerator performs proton-proton, proton-ion, and ion-ion collisions at four locations along the LHC. A detector is placed at each collision point to record kinematic measurements of the products produced. The ATLAS and CMS detectors are general-purpose detectors used to study a wide range of physical phenomena [10, 30]. In contrast, the ALICE and LHCb detectors heavy ion physics and flavor physics [11, 14].

The LHC contains two rings that accelerate the particles in opposite directions and has a max center-of-mass (c.o.m) energy for pp-collisions of 14 TeV. The c.o.m. energy slowly increased over the years starting in November 2009. In 2009-2011 the c.o.m. energy for pp-collisions was at 7 TeV and was raised to 8 TeV during 2012. This period is called Run 1. The c.o.m energy increased to 13 TeV for 2015-2019 after a series of upgrades following Run 1. This data-taking period is called Run 2.

2.1.1 Accelerating the Protons

Hydrogen is ionized to create the protons for the accelerator. These protons pass through several sub-accelerators to increase the energy until they finally reach the LHC. Figure 6 shows all the accelerators at the CERN facility. The initial accelerator is the linear accelerator LINAC 2 [19]. This accelerator uses drift tubes and RF powering to accelerate the protons to 50 MeV. Pulsed quadrupoles in the $\pm$ configuration keep the beam focused.

Three separate synchrotron machines then accelerate the protons before being injected into the LHC. The first is the Proton Synchrotron Booster (PSB) which contains four superimposed rings with a radius of 25 meters. The PSB accelerates the protons from 50 MeV to 1.4 GeV. Protons are then accelerated to an energy of

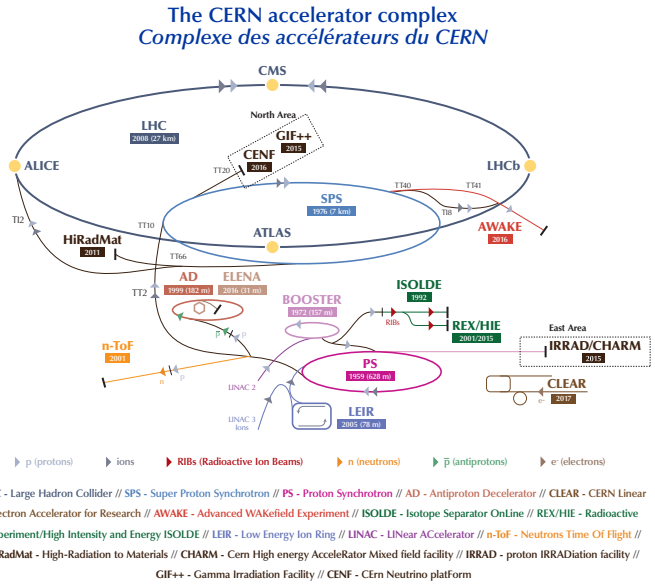

Figure 6: Accelerator complex at CERN showing all the accelerators and their position relative to one another. The acceleration chain for the LHC is LINAC 2 to BOOSTER to PS to SPS to LHC [34].

28 GeV by the Proton Synchrotron (PS), a 628-meter-long accelerator in circumference. The Super Proton Synchrotron (SPS) is the final accelerator before the LHC. Previously the highest-powered accelerator, this accelerator boosts the proton energy to 450 GeV [35].

2.1.2 Luminosity

When the LHC operates at peak luminosity, each ring can contain 2808 individual bunches of protons. These bunches are separated in time by 25 ns and have 1.15×10^{11} protons. Before entering the collision point, the proton bunches pass through focusing quadrupoles to reduce the width of the bunch [20]. Assuming both bunches have a Gaussian spread after the quadrupoles, the instantaneous luminosity is

$$\mathcal{L} = \frac{N_b^2 n_b f_{\text{rev}}}{4\pi\sigma_x\sigma_y} F \tag{2.1.1}$$

where N_b is the number of protons in each bunch, n_b is the number of bunches, f_{rev} is the frequency of revolution for the bunches, $\sigma_{x/y}$ is the spread of the bunch in each direction, and F is a suppression factor for if the angle of crossing is non-zero [36].

After the LHC has undergone a "Fill", the LHC is designed to have a peak instantaneous luminosity of 1.0×10^{34} cm^{-2} s^{-1}, which Run 2 was able to surpass. As the LHC runs, the number of protons in each bunch decreases, resulting in the instantaneous luminosity decreasing. Integrating the instantaneous luminosity over the time the LHC is running provides the total integrated luminosity

$$L = \int \mathcal{L}\, dt \tag{2.1.2}$$

Throughout Run 2, the LHC delivered a total integrated luminosity of 156 fb^{-1} [9]. ATLAS only recorded 147 fb^{-1} of the total luminosity delivered by the LHC and qualified 140 fb^{-1} suitable for physics analysis. Figure 7 shows the luminosity produced by the LHC and recorded by ATLAS.

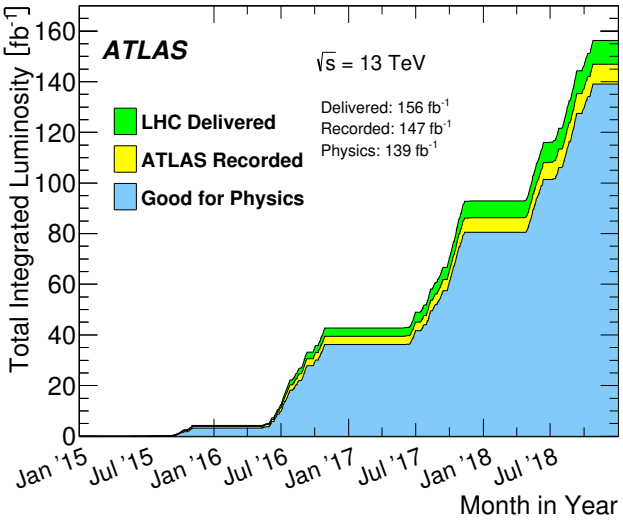

Figure 7: Figure showing the breakdown of the luminosity delivered by the LHC, recorded by ATLAS, and qualified as good to use for physics analyses as a function of data taking period [9].

When the bunches collide in the detector, multiple protons collide simultaneously, called pile-up. The amount of pile-up for each data-taking period varies. Figure 8 shows the luminosity-weighted pile-up distribution for each data-taking period.

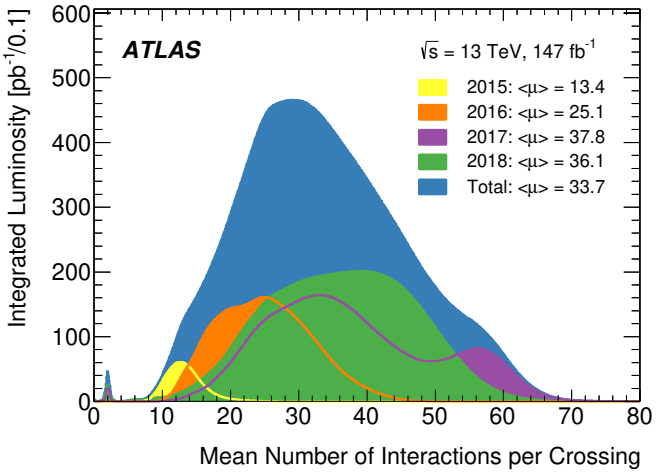

Figure 8: Figure showing the luminosity-weighted pileup distributiion for each data taking year [9].

2.2 The ATLAS Detector

The ATLAS (A Toroidal LHC Apparatus) detector [10] is one of the two luminosity experiments on the LHC ring. The detector is in the shape of a cylinder measuring 46 m in length and 25 m in diameter with forward-backward symmetry. There are three concentric subsystems within ATLAS to measure different properties of the particles produced in collisions and provide coverage for most of the solid angle. A computer-generated model of the ATLAS detector with a slice removed, with people for scale, is shown in Figure 9.

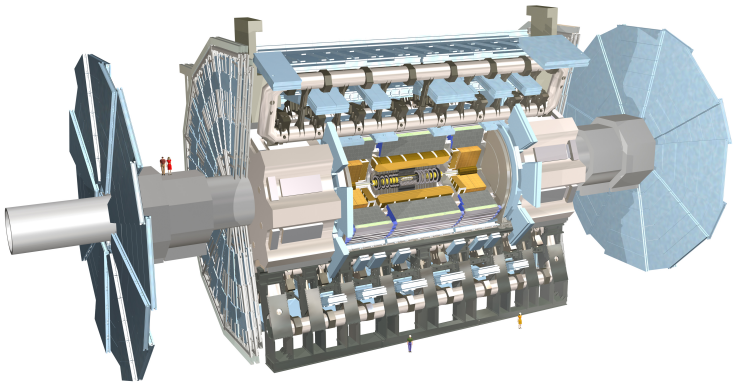

Figure 9: Computer-generated model of the ATLAS detector with a slice taken removed showing the subsystems. People have been added to the figure to show the relative size of the detector [34].

A cylindrical coordinate system defines the interaction points inside the detector. A right-handed cartesian coordinate system with the origin at the collision point, the x-axis pointing toward the center of the LHC, and the y-axis pointing straight up is the basis for the cylindrical coordinate system. Two angles define the positions within the detector. The first is the azimuthal angle ϕ. The second is the pseudorapidity (η), defined as

$$\eta = -\ln\left(\tan\left(\frac{\theta}{2}\right)\right) \tag{2.2.1}$$

where θ is the longitudinal angle measured between the z-axis and the trajectory of the particle produced. Pseudorapidity is used instead of θ for its close relationship to rapidity $\left(y = \frac{1}{2}\ln\left(\frac{E+p_z}{E-p_z}\right)\right)$, where Δy is invariant under Lorentz boosts. The pseudorapidity and rapidity values are approximately equal in the limit of $E >> m$. η and ϕ provide a Lorentz-invariant coordinate system with distance measurements defined as $R = \sqrt{(\Delta\eta)^2 + (\Delta\phi)^2}$.

The three subsystems within the ATLAS detector are the Inner Detector (ID), the calorimeters, and the muon spectrometers. The ID is closest to the collision point and measures the trajectory of charged particles created in collisions. Calorimeters measure the energy of electromagnetic and hadronic particles. The final subsystem is the muon spectrometer. This system measures the path of muons and combines the information with the ID to determine the energy and trajectory. Each subsystem contains a *barrel* region which is the cylindrical component of the subsystem at low η, and an *endcap* region, which are disk-shaped components at higher η. Neutrinos are a common particle produces in the interactions but do not interact with the detector. Important information about these particles can be calculated and is called the Missing Transverse Momentum $\left(E_{\mathrm{T}}^{\mathrm{miss}}\right)$ and is the negative vector sum of all other transverse momenta.

The ATLAS detector has two different magnetic fields and computational components for trigger and data acquisition (TDAQ). A solenoid magnet is just outside the ID, and a toroid magnet is around the muon spectrometer, which causes charged particles to bend as they travel through the magnetic fields. The TDAQ system filters out unwanted events and stores the wanted events.

2.2.1 The Inner Detector

The Inner Detector (ID) [10] is the closest subsystem to the interaction point within ATLAS. The purpose of the ID is to track the path of any charged particles created in a pp-collision. This subsystem sits inside a 2 T solenoid magnet that bends the trajectory of the charged particles. The information recorded by this system reconstructs tracks of the charged particles, and the reconstructed paths help define the transverse momentum of any charged particle created. Three subsystems make up the ID. The inner two systems, the Pixel detector and the Semi-conductor tracker use silicon-based sensors to track the path of the particles. The outermost system in the ID, the Transition Radiation Tracker, uses the ionization of a noble gas to reconstruct the trajectory. Figure 10 shows the ID layout and a representation of the track reconstruction from signals in the detector.

Pixel Detector

The innermost system in the ID is the Pixel detector which provides high-efficiency tracking for $|\eta| < 2.5$ [10]. During Run 1 of ATLAS, the Pixel detector contained only three layers of sensors in the barrel region and three endcap disks on either side. The radius of the barrel layers was 50.5, 88.5, and 122.5 mm from the beam pipe. The disks had sensors at a radius of 88.8 and 149.6 mm. There are a total of 1744 pixel sensors within the detector with a pixel size of $50 \times 400 \times 250$ μm. This results in 46,080 readout channels within the detector for tracking. Figure 11 shows the location of the barrel layers and endcap rings.

The Insertable B-Layer (IBL) [21] was placed in the detector for Run 2. The IBL added one extra layer of sensors in the barrel region at a radius of 33.3 mm from the center of the beam pipe. This extra layer of sensors added 896 sensors with a size of

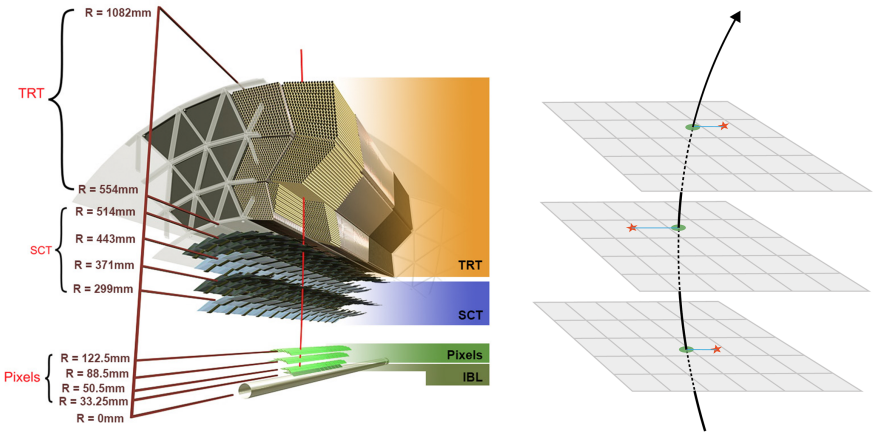

Figure 10: Diagram of the Inner Detector layout showing the subsystems in respect to the beam pipe. This figure also shows a schematic of how tracks are reconstructed. The stars represent where the particle passed through the detector and the dots are where the reconstructed track passes the sensors [34].

$50 \times 250 \times 250$ μm to the Pixel detector to help with tracking, providing excellent power in identifying particles like top and bottom quarks.

Semi-Conductor Tracker

The following system of the ID is the Semi-Conductor Tracker (SCT) [10]. This system contains four layers in the barrel region and nine rings in the end cap. The layers range from a radius of 299 mm to 514 mm. Like the Pixel Detector, this detector uses silicon sensors to record the path of the outgoing particles, but the silicon in the sensors are strips with a size of $80 \times 120,000 \times 258$ μm. This system uses a total of 15,912 sensors with 768 strips per sensor. Figure 11 shows the location of the barrel layers, and endcap rings for the SCT.

Transition Radiation Tracker

The final system in the ID is the Transition Radiation Tracker (TRT) [27]. This detector utilizes a mixture of 70% Xenon, 27% Carbon dioxide, and 3% Oxygen gas as the ionization material. In the center of each tube is a 31 μm gold-plated tungsten anode, which collects the freed electrons from the ionized gas. The barrel region of the system is composed of 73 layers of straws organized in 3 concentric rings totaling 52,544 straws in the entire barrel region, covering the radius range of 560 to 1080 mm. Each straw is 142.4 cm long and runs parallel to the beam pipe. The endcaps consist of two types of rings, with every ring containing eight layers of 768 straws, each of length 36 cm oriented in the r-ϕ plane. The first type of ring has an empty 4 mm gap between each layer, while the second type contains a 16 mm space where 12 mm of it includes the gas mixture. Each side of the endcap comprises 12 of the 4 mm gap rings and eight of the 16 mm gap rings. While the spatial resolution of the TRT is the worst of all the subsystems, it has practical use in differentiating particles, mainly

electrons from pions, by utilizing the transition radiation emission depending on the Loretz γ-factor. Figure 11 shows the layout of the TRT.

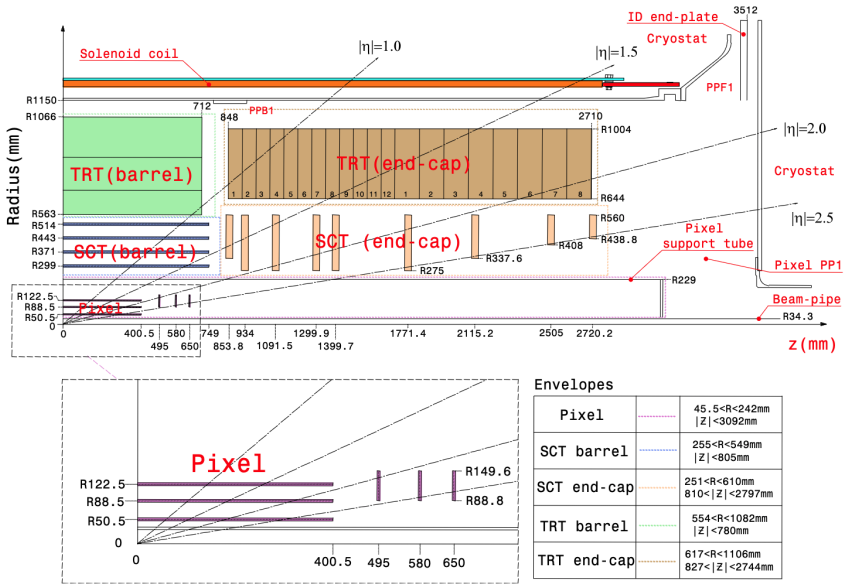

Figure 11: This schematic shows the layout of the Inner Detector for both the barrel and endcap region during Run 1. It shows the pseudorapidity coverage of each system and the radius each component is at [10].

2.2.2 Calorimeters

The calorimeters are the next subsystem in ATLAS after the ID. This system sits outside the solenoid and is responsible for measuring the energy of any outgoing particles. The electromagnetic calorimeter is the first in this subsystem and measures the energy of electromagnetic particles, such as electrons and photons. The hadronic calorimeter is next and measures the energy of hadronic products from the collision. Both are sampling calorimeters alternating between an active layer and a sampling layer. The active layer interacts with the products from the collision to create secondary particles measured by the sampling layer. A calibration converts the information recorded from the sampling layer to the energy. Figure 12 shows the different calorimeter components.

Electromagnetic Calorimeter

The electromagnet calorimeter [10] is the first of the calorimeters after the ID. This detector utilizes lead plates sandwiched between stainless-steel sheets as the absorber and liquid argon as the sampling material. Copper electrodes are in gaps in the absorber for the read-out. The absorbers have an accordion geometry to provide full coverage in ϕ and fast signal extraction. The barrel region of the electromagnet calorimeter contains two cylinders split by positive and negative η. This calorimeter region is called the LAr electromagnetic barrel and covers $0 < |\eta| < 1.475$ and ranges

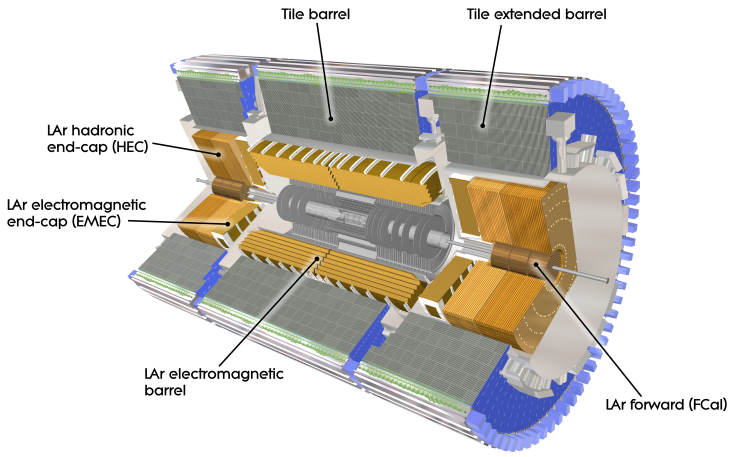

Figure 12: Figure showing the different components of the ATLAS calorimeters provided by the ATLAS experiment [34].

from 2.8 m to 4 m away from the beam pipe. There are three layers in the barrel region with decreasing granularity as the distance from the beam pipe increases. Figure 13 shows a schematic of a calorimeter geometry at $\eta = 0$. The end-cap calorimeters contain one wheel on either side of the barrel covering the range $1.375 < |\eta| < 3.2$. The gap between the end-cap and barrel calorimeters is filled with a liquid argon presampler to help improve the measurement in this region. Each end-cap contains two co-axial wheels with a 3 mm gap at $|\eta| = 2.5$. This calorimeter region is called the LAr electromagnetic end-cap.

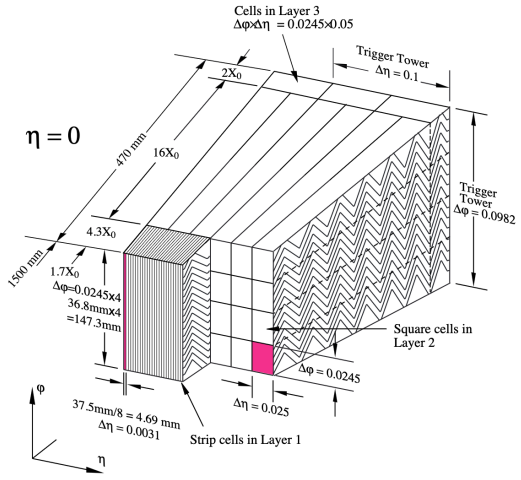

Figure 13: Drawing of the three LAr calorimeter layers and the granularity for each layer [10].

Hadronic Calorimeter

The hadronic calorimeter [10] is a sampling calorimeter with the tile barrel, the LAr hadronic end-cap (HEC), and the LAr forward colorimeter (FCal). The tile calorimeters use steel as the absorber and a scintillator as the sample material. A wavelength-shifting fiber carries the signals from the scintillator to a photomultiplier tube. The output from the photomultiplier tube is the signal recorded from the system. Figure 14 shows the layout of the tile barrel. The tile barrel contains a central 5.8 m component called the tile barrel and two 2.6 m tile extended barrels on either side. Combined, these cover $|\eta| < 1.7$. The HEC and FCAl use a copper absorber with a liquid argon sampler. The HEC has two wheels and covers $1.5 < |\eta| < 3.2$, while the FCal has three cylinders covering $3.1 < |\eta| < 4.9$. Since the FCal is at high η, it experiences a larger flux of particles than the other regions. The gaps filled with liquid argon are reduced in size to negate ion buildup. The HEC and FCal are placed within the same cryostat, resulting in a highly coupled system that minimizes the energy loss from the cracks between the systems.

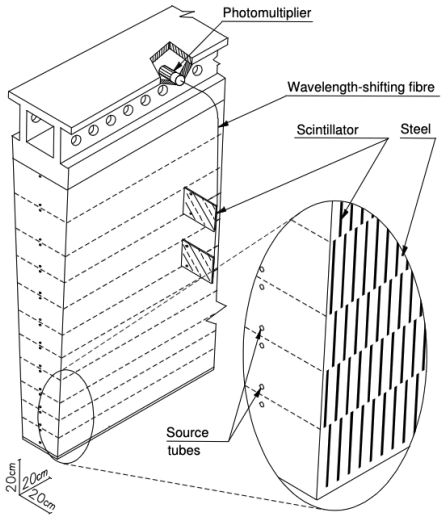

Figure 14: Schematic of the tile barrel calorimeter showing the absorber and sampling layers, the wavelength shifting fiber, and the photomultiplier tube [10].

2.2.3 Muon Spectrometer

The final subsystem in ATLAS is the muon spectrometer [10]. This system contains three concentric cylinders at a radius of 5 m, 7.5 m, and 10 m in the barrel region and four disks at roughly $|z|$ of 7.4 m, 10.8 m, 14 m, and 21.5 m. Figure 15 shows the location of the barrel components in green and the disks in light blue. These cylinders and disks use Monitored Drift Tubes (MDTs) with a radius of about 30 mm filled with 93% Argon gas and 7% carbon dioxide covering $|\eta| < 2.7$. Due to a significant drift time in the MDTs, the first end cap disk uses Cathode-Strip Chambers (CSC) for $|\eta| > 2$ where the flux of particles is the highest. The CSCs have cathodes perpendicular to the wires in the center of the drift tube, and the charge induced on

the cathodes provides the signal. The barrel region of the muon spectrometer is inside eight coils of a superconducting toroid magnet, with the end-cap disks being outside the coils. This detector provides a resolution of 10% for particles with a transverse momentum of 1 TeV.

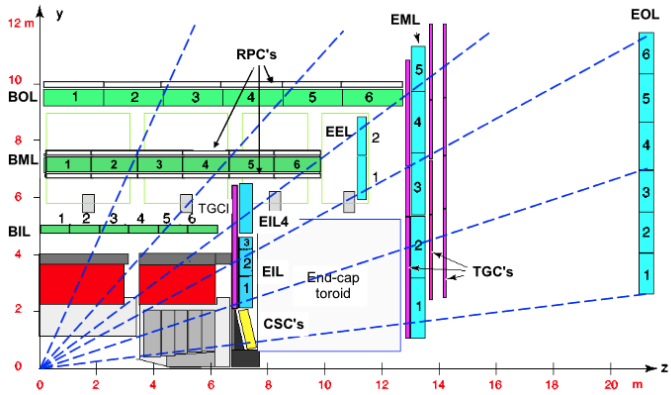

Figure 15: Schematic showing the cross-section of the muon spectrometer. The barrel region of the system is shown in green while the end cap disks are in light blue [34].

2.2.4 Trigger and Data Aquisition

Once ATLAS detects the particles, the trigger and data acquisition (TDAQ) system processes the signals [10]. The trigger is a two-level process that takes information from each subsystem and filters events that are not interesting. The Level-1 (L1) trigger selects an event based on calorimeters and muon spectrometer data. The L1 Calorimeter Trigger (L1Calo) looks for events with a large total transverse energy or events which contain a high transverse energy electron, photon, jet, hadronically decaying τ-lepton, or large $E_{\mathrm{T}}^{\mathrm{miss}}$. The L1 muon trigger searches for muons that pass one of the transverse momentum thresholds. The maximum event rate for the L1 trigger is 75 kHz. The second stage of the trigger is the High-Level Trigger (HLT) which combines a Level-2 trigger and an event filter. The Level-2 (L2) trigger takes information from the L1 trigger and uses coordinates, energy, and type of signatures to limit the data transferred from the detector. The L2 trigger reduces the event rate to 3.5 kHz. The event filter uses fully reconstructed events and offline analysis procedures to reduce the event rate to about 200 Hz. If the event passes the HLT, it is then moved to permanent event storage by the DAQ.

CHAPTER III

Object Reconstruction

The signals recorded by the subsystems in the ATLAS detector are used as inputs to algorithms to define the energy-momentum four vectors for electrons, muons, photons, and jets. The output of the algorithms is what analyses use. This chapter discusses how the algorithms define and reconstruct the physics objects.

3.1 Electrons and Photons

Electrons and photons are reconstructed by the ATLAS detector using information recorded by the Electromagnetic Calorimeter (EMcal) and the Inner Detector (ID) [26]. Electrons and photons undergo reconstruction together since electrons emit photons from bremsstrahlung radiation, and photons can create electrons from pair production. First, a clustering algorithm uses the cells in the EMcal to define areas of interest within the detector. The ID then reconstructs the tracks of charged particles from "hits" within the subsystems. The matching of tracks to the energy clusters defines electron and photon candidates.

The EMcal cell significance is the crucial variable for the energy clustering algorithm. The significance is measured energy in a calorimeter cell divided by the expected noise of the cell. The clustering algorithm starts with cells with a significance of at least 4. The clustering continues by combining any neighboring cell with a significance of at least 2. Finally, cells with a significance of at least 0 or combined with the energy cluster. The algorithm then finds local maxima within the cell of an energy of at least 500 MeV. The cluster is broken into multiple clusters if a maximum has at least four neighboring cells with lower energy. These new clusters are called topological clusters (topo-clusters). A cell's energy is split between two topo-clusters if both use it based on the distance from the maximum.

The locations of the topo-clusters in the EMcal define regions of interest within the ID. The track reconstruction process starts with the inside-out reconstruction algorithm within these regions of interest [32]. Hits recorded by the pixel detector and the semi-conductor tracker create spacepoints which are three-dimensional coordinates within the sensor. Spacepoints are combined to generate track seeds to identify areas within the detector for track reconstruction. Track candidates are reconstructed by following the trajectory of a charged particle traveling in a magnetic. An algorithm scores each track candidate and removes any track which does not receive a score above a specific cutoff. If no track candidates remain in the region of interest, the procedure repeats, allowing for more energy loss for each track [26]. The

track remaining track candidates are then loosely matched to the topo-clusters. A Gaussian Sum Filter fitter performs a final fit with the matched tracks. If the algorithm matches multiple tracks to a topo-cluster, the track with the highest number of hits in the pixel detector closest to the topo-cluster is selected.

Photon reconstruction starts by defining conversion vertices from tracks from the GSF fit, where vertices reconstructed from two tracks must be consistent with a massless particle [26]. One-track vertices are reconstructed as well and are generally a result of a track without hits in the innermost layers of the ID. The tracks must then be identified as tracks from an electron from the TFT to increase the purity of the converted photon identification. The algorithm prefers double-track vertices with the most hits in the silicon detector with the smaller conversion radius if multiple conversion vertices match the topo-cluster.

3.2 Muons

Muons are particles that are massive enough to travel through all the subsystems within ATLAS and only leave minimal energy in the calorimeters. The information recorded by the ID and the Muon Spectrometer (MS) is the main inputs used by the reconstruction algorithm [18]. The reconstruction of muons starts with the MS and then matches these tracks to those in the ID.

The first step in muon reconstruction is to define short straight tracks from hits inside the MS. These tracks are then expanded by using the direction from the collision point and assuming a parabolic trajectory as a first-order approximation of a muon traveling through a magnetic field. A χ^2 fit to the actual trajectory of a muon in a magnetic field creates a more accurate track. More hits in the MS are added to this trajectory if they are consistent with the fit. The algorithm prefers a track with better reconstruction if serval tracks share hits. This fit then considers the minimal energy loss in the calorimeters to create the final track in the MS.

The tracks defined by the MS are extrapolated to the ID and matched to tracks created by the ID reconstruction algorithm. Only tracks with the highest probability are kept. If there are no tracks after the matching, the reconstructed ID tracks are extrapolated to the MS. If the extrapolated ID track is aligned loosely to three hits in MS, the ID track defines the muon trajectory. The final muon definition combines this track with the energy left in the calorimeters and the hits in the MS.

3.3 Jets

The majority of the collisions at the LHC result in quarks or gluons (partons). Due to color confinement, these particles cannot exist independently and undergo a parton shower and hadronization. The parton shower and hadronization is a process where more patrons form from the vacuum until the partons couple together to create stable hadrons. These stable hadrons travel through the detector, leaving all the energy in the hadronic calorimeter. The cells in the hadronic calorimeter use the same topo-clusters clustering algorithm defined for electrons. Small-radius (small-R) and

large-radius (large-R) jets are created by clustering the topo-clusters using different parameters.

3.3.1 Small-R Jets

The particle flow algorithm uses tracking information from the ID and topo-clusters from the hadronic calorimeter to create small-R jets [2]. The jets reconstructed with the particle flow algorithm are called pflow jets. The algorithm requires tracks from the ID to pass a series of selections. The tracks must have at least nine hits in the silicon layers of the ID with no missing hits in the pixel detector, be in the $|\eta| < 2.5$ region of ATLAS, have a transverse momentum between 0.5 and 40 GeV, and cannot be matched to an electron or muon candidate.

The tracking algorithm extrapolates the track to the second layer of the EMcal, and an angular distance is calculated between the track and the topo-clusters using

$$\Delta R' = \sqrt{\left(\frac{\Delta\phi}{\sigma_\phi}\right)^2 + \left(\frac{\Delta\eta}{\sigma_\eta}\right)^2} \tag{3.3.1}$$

where σ_ϕ and σ_η are the width of the topo-cluster. The particle flow algorithm performs a preliminary selection where the topo-cluster's energy divided by the track's p_{T} is greater than 0.1. After this selection, the closest track to the topo-cluster is the track for that cluster. If no topo-cluster is within $\Delta R' = 1.46$ to the track, the track is assumed not to have created a topo-cluster. Each matched track is passed to an algorithm to determine if the particle's energy created by the track is within more than one topo-clusters. The algorithm combines topo-clusters in a cone with a radius of 0.2 if the algorithm determines the energy is not in one topo-cluster. A cell-by-cell subtraction removes the energy from each track and energy that entered the topo-cluster from a different topo-cluster. The anti-k_{T} algorithm clusters the remaining topo-cluster and the topo-cluster, which are matched to tracks, using a radius parameter 0.4.

3.3.2 Large-R Jets

Topo-clusters originating from pile-up events are first removed by an algorithm when creating large-R jets [38]. The remaining topo-clusters are combined using the anti-k_{T} clustering algorithms with a radius parameter 1.0. The large-R jets undergo trimming to remove any surviving pile-up topo-clusters. The k_{T} algorithm, with a radius parameter of 0.2, reclusters the calorimeter cells within the untrimmed large-R jet. Any reclustered cells with a fraction of the large-R jet transverse momentum less than 0.05 are from the final large-R jet.

3.3.3 Jet Calibration

The calibration for small-R and large-R jets follows the same general process. A calibration is applied to Monte Carlo simulated data to the truth level, and then a residual In situ calibration is performed to calibrate data to the calibrated MC. The In

situ calibration step contains three parts where the leading jet recoils against a system of well-calibrated objects. The three objects are photons (γ+Jet), Z boson decaying to two electrons or two muons (Z+Jets), and a system of fully calibrated small-R jets (multijet balance). These three calibrations are combined to span an extensive momentum range for the leading jet. The multijet balance is crucial because it is the only process to calibrate high-momentum jets. The derivation of the multijet balance for large-R jets was part of the work for this dissertation.

The multijet balance uses events where the large-R jet with the highest transverse momentum recoils against a fully calibrated small-R jet system. There are specific requirements for each event's jets in the recoil system. Any jet used in the recoil system must have an angular separation from the lead g large-R jet greater than 1.0. This way, no calorimeter cell is double-counted. Next, each jet's p_{T} must be greater than the p_{T} threshold of 25 GeV. To ensure that one jet in the recoil system does not have all the p_{T} of the system, a selection is applied to the p_{T} asymmetry of the recoil system. The p_{T} asymmetry is defined as

$$\mathscr{A}^{p_{\mathrm{T}}} = \frac{p_{\mathrm{T}}^{\text{lead recoil,jet}}}{p_{\mathrm{T}}^{\text{recoil system}}} \tag{3.3.2}$$

and must be less than 0.8. Another angular distance selection is placed on the jets to ensure that the large-R jet is the only jet in one hemicylinder of the detector. The distance between the closest small-R and large-R jet (β) must exceed 1.5. The final selection depends on the difference in ϕ-angle between the large-R jet and the vector sum of all the small-R jets in the recoil system (α). To ensure the large-R jet and the recoils system are back-to-back $|\alpha - \pi| < 0.3$. Each selection has an up and a down variation for the uncertainty calculation. Table 1 summarizes the selection requirements.

Table 1: Selection requirements for events to be included in the calulation of the multijet balance.

Selection	Noiminal Value	Down Systematic	Up Systematic
p_{T} Threshold	25 GeV	20 GeV	30 GeV
$\mathscr{A}^{p_{\mathrm{T}}}$	< 0.8	< 0.7	< 0.9
β	> 1.5	> 1.0	> 2.0
$\lvert\alpha - \pi\rvert$	< 0.3	< 0.2	< 0.4

The response for each event is calculated for each event that passes the selection requirements. The response is defined as the p_{T} of the object being calibrated divided by the p_{T} of the reference object $\left(\mathscr{R} = \frac{p_{\mathrm{T}}^{large-R\,jet}}{p_{\mathrm{T}}^{\text{recoil}}}\right)$. The response of each event response is then binned in terms of $p_{\mathrm{T}}^{\text{ref}}$. A Gaussian fits the responses, and the mean of the fit is the response of that p_{T} range. Figure 16 shows the fitting of the response distribution for the bins of $p_{\mathrm{T}}^{\text{ref}}$.

A new distribution is made which plots the average response $\langle\mathscr{R}\rangle$ vs $p_{\mathrm{T}}^{\text{recoil}}$. This procedure is done for both data and MC. The correction for the data is the ratio of MC to data for the $\langle\mathscr{R}\rangle$ distribution. The uncertainty for the calibration is determined

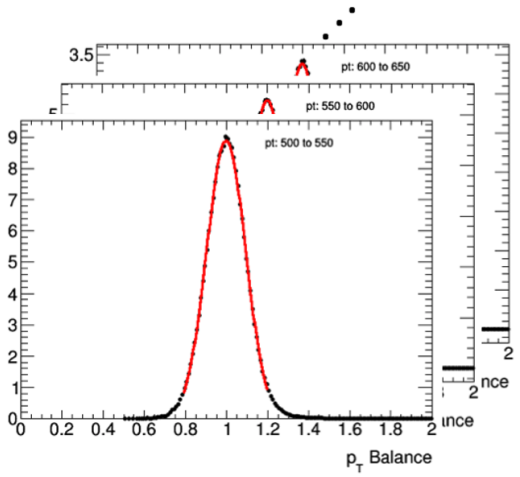

Figure 16: Gaussian fits to the response for different bins of the transverse momentum of the recoil system. The mean value of the fit is taken as the nominal value.

by calculating the difference between the nominal correction and the correction if a parameter is changed. Figure 17 shows the nominal $\langle \mathscr{R} \rangle$ distribution and the total uncertainty for the correction.

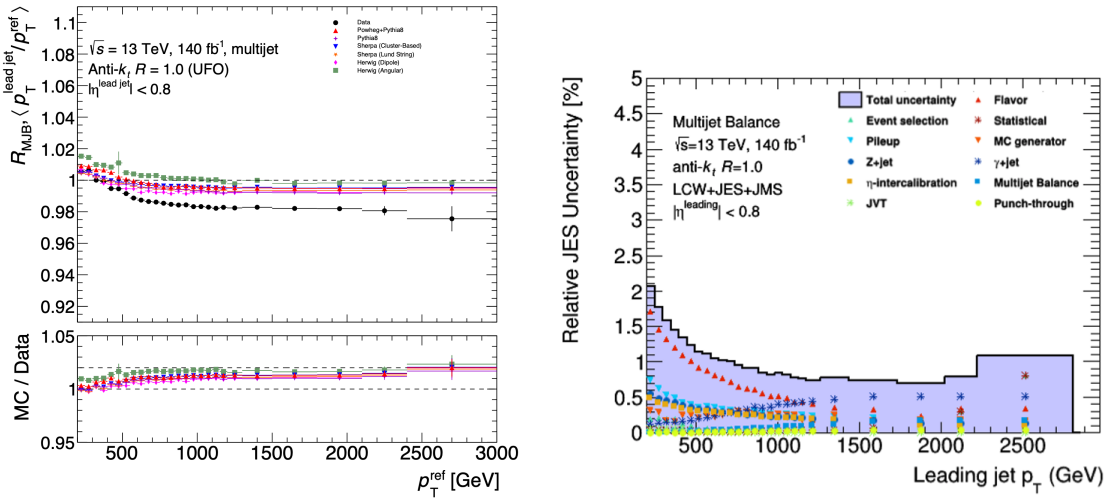

Figure 17: Left plot shows the mean response as a function of the recoil system transverse momentum. Right plot shows the total uncertainty on the calibration factor as a function of large-R jet transverse momentum.

CHAPTER IV

Wq+X Analysis

This chapter discusses an analysis searching for the pair production of vector-like quark (VLQ) partners to standard model (SM) light quarks. This analysis looks for VLQs that decay to the semi-leptonic Wq+X final state. One of the produced VLQ is required to decay to a leptonically decaying W-boson and a light quark, while the other decays to a hadronically decaying boson and light quark. This analysis is optimized for when the second VLQ decays to a hadronically decaying W-boson using a W-tagging algorithm provided by the ATLAS collaboration. Figure 18 shows the Feynman diagram for this analysis.

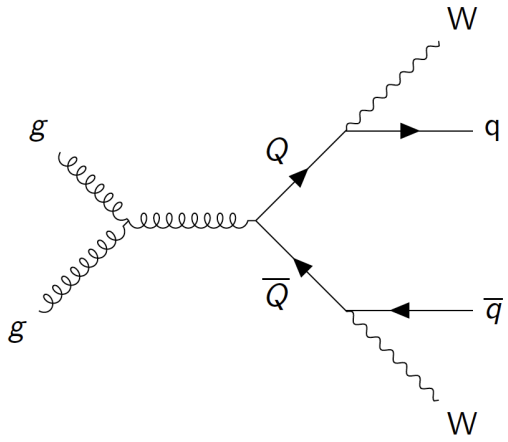

Figure 18: Feynamn diagram of the signal for this analysis.

4.1 Analysis Strategy

The analysis uses a strategy that takes advantage of the kinematic differences of the VLQ decay products to calculate the experimental cross-section of VLQ production as a function of mass. Monte Carlo (MC) simulation estimates the kinematics of SM processes, and the VLQ decays. Signal regions (SRs) are created to be sensitive to the decay of the VLQs by removing as many SM events as possible. Data-driven corrections are calculated and applied to specific MC simulations to fix any mis-modeling. Finally, a statistical fit is then done in the SRs between the data and the corrected MC to calculate the experimental cross-section of VLQ production as a function of the mass of the VLQ. The statistical fit uses a variable with good separation between the background and the signal called the discriminating variable.

This analysis uses the mass of the leptonically decaying VLQ candidate $\left(M_{\mathrm{VLQ}}^{\mathrm{lep}}\right)$ as the discriminating variable.

4.2 Monte Carlo Simulation

The MC used by the ATLAS collaboration is all created following a general strategy [37]. The first step is "Event Generation." This step simulates the creation of the process from a pp collision and the decay of the particles. This generation simulates the decay of all particles that decay before reaching the ATLAS detector. For some processes, the parton shower and hadronization simulation is done by a separate generator. GEANT 4 [12] then simulates the passage of these stable particles through the ATLAS detector. The simulated signals of the ATLAS subsystems are then digitized. The reconstruction algorithms use the digitized signals as described in Chapter III. The processes in this analysis are:

- W+Jets: Production of a leptonically decaying W-boson and extra jets
- $t\bar{t}$: Pair production of SM top quarks decaying with at least one lepton
- Single top: Production of one SM top quark
- Z+Jets: Production of a leptonically decaying W-boson and extra jets
- ttV: Pair production of SM top quarks along with a vector boson (W or Z)
- Disboson: Production of two vector bosons
- VH: Production of a vector boson along with a Higgs boson
- Multijet: Collision creating nothing but jets
- VLQ Signal: Pair production of vector-like quarks

The events from Z+Jets, ttV, diboson, and VH are combined into one process called "Other Bkgs" because few events pass all the selections. The specific details for the MC generation can be found in the publication for this analysis [24].

4.3 Event Selection

Events must go through different selections to reduce the number of events that are not kinematically close to the signal process. The first selection is the "primary selection." This selection aims to remove any event with no similarities to the signal process, such as any event without a lepton. The "preselection" applies stronger requirements to start rejecting SM events. Events that pass the preselection are sorted into different regions. These regions are called "control regions" (CRs), "validation regions" (VRs), and "signal regions" (SRs). Every region must be orthogonal to each other, so no events are in multiple regions. CRs are used to calculate data-driven corrections to a specific MC process. CRs must be pure in one SM process and contain no events from

the signal to avoid biasing the correction. VRs are dominated by one SM process and contain no events from the signal process to check the data-to-MC agreement after the corrections. SRs are regions that are the most sensitive to the signal.

4.3.1 Primary Selection

There is a collision in the ATLAS detector every 25 ns. For a collision in the ATLAS detector to be stored, it must activate a trigger. This analysis used events that activated either the single lepton trigger or the $E_{\mathrm{T}}^{\mathrm{miss}}$ trigger. The single lepton trigger is triggered if an event has a reconstructed lepton. Since the ATLAS detector is not 100% efficient at reconstructing leptons, a scale factor is applied to the MC to model the trigger efficiency correctly. Events activate the $E_{\mathrm{T}}^{\mathrm{miss}}$ trigger if the event has a large $E_{\mathrm{T}}^{\mathrm{miss}}$. A study found that 100% of data events that activated the single lepton trigger and had a $E_{\mathrm{T}}^{\mathrm{miss}}$ of at least 250 GeV passed the $E_{\mathrm{T}}^{\mathrm{miss}}$ trigger. Figure 19 shows the fraction of events that activated the single lepton trigger that also passed the $E_{\mathrm{T}}^{\mathrm{miss}}$ trigger as a function of the $E_{\mathrm{T}}^{\mathrm{miss}}$ of the event. This analysis required that each event have a $E_{\mathrm{T}}^{\mathrm{miss}}$ of 250 GeV such that it would be in the regime that the $E_{\mathrm{T}}^{\mathrm{miss}}$ trigger was fully efficient.

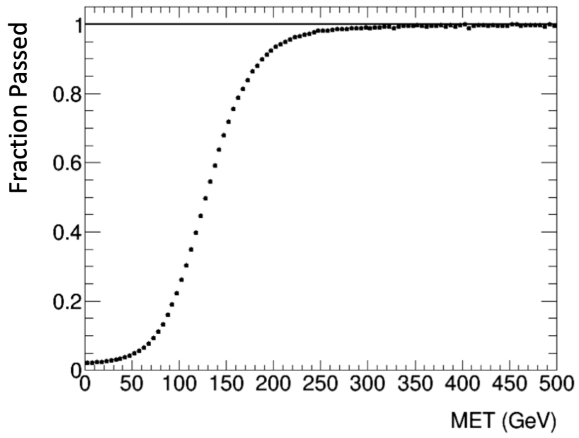

Figure 19: Plot showing the fraction of events which pass the $E_{\mathrm{T}}^{\mathrm{miss}}$ trigger as a function of the $E_{\mathrm{T}}^{\mathrm{miss}}$ of the event. This plot shows that 100% of events wiht a $E_{\mathrm{T}}^{\mathrm{miss}}$ of at least 250 GeV pass the $E_{\mathrm{T}}^{\mathrm{miss}}$ trigger.

This selection removes events that are not close to the decay of the signal process. For an event to pass this selection, it must have exactly one electron with a transverse momentum p_{T} of 27 GeV or exactly one muon with a p_{T} of 25 GeV. Events must have at least three small-R jets with a p_{T} of at least 25 GeV. These are the lowest calibrated p_{T} for these objects. These requirements account for the leptonically decaying W boson, the quarks from the decay of the VLQs, and having at least one quark from the hadronically decaying W boson. Table 2 summarizes the primary selection.

Table 2: Summary of the primary selection requirements.

Primary Selection	
Variable	Cut
$E_{\mathrm{T}}^{\mathrm{miss}}$	$\geq$250 GeV
N_{lepton}	$== 1$
$p_{\mathrm{T}}^{\mathrm{el(mu)}}$	$\geq$ 27(25) GeV
$N_{\text{small-R jets}}$	≥ 3
$p_{\mathrm{T}}^{\text{small-R jets}}$	$\geq$ 25 GeV

4.3.2 Preselection

The primary selection removed any event that does not resemble the final state of the signal. The preselection further reduces the number of events by checking there are enough objects to reconstruct two VLQ candidates. Selections are also made on the p_{T} of objects to remove events that are not kinematically similar to the signal process. The previous version of this analysis has excluded VLQs with a mass below 800 GeV [8], so the decay products from the decay of the VLQ are expected to have a large p_{T} (boosted).

The quarks resulting from the hadronic decay of the W boson are expected to be collimated since the boson will be boosted from the massive VLQ, so a large-R jet will likely capture the energy from both quarks. Each event must have at least one large-R jet so there is a candidate for the hadronically decaying W boson. The ATLAS collaboration provides an algorithm that identifies large-R jets as being from the decay of a W boson within some probability called a W-tagger. The W-tagger calibration is only valid for large-R jets with a p_{T} of at least 200 GeV, so the hadronic W-boson candidate must have a p_{T} above this threshold. Along with requiring a large-R jet, the event must also have at least two small-R jets for the quarks resulting from the decay of the VLQs. The small-R jets must have a radial distance of at least one from the large-R jet to ensure that calorimeter clusters are not double-counted (overlap removal). The preselection also has requirements for the p_{T} of the small-R jet with the highest p_{T} (leading) and the lepton. The leading small-R jet must have a p_{T} of at least 200 GeV, and the lepton must have a p_{T} of at least 60 GeV. Finally, the event must have a $E_{\mathrm{T}}^{\mathrm{miss}}$ of at least 250 GeV to double-check that the event is in the regime of the trigger. Table 3 summarizes the selections of the preselection.

4.3.3 Reconstuction of VLQ Candidates

Any event which passes the preselection undergoes an algorithm to reconstruct two VLQ candidates. This algorithm identifies a large-R jet as the hadronically decaying W boson. The lepton is combined with a reconstructed neutrino to create the leptonically decaying W boson. The W boson candidates are combined with the small-R

Table 3: Summary of the preselction requirements.

Preselection	
Variable	Cut
$N_{\text{large-R jets}}$	≥ 1
$N_{\text{small-R jets}}^{\text{overlap removal}}$	≥ 2
$p_{\text{T}}^{\text{leading small-R jet}}$	≥ 200 GeV
$p_{\text{T}}^{\text{lepton}}$	≥ 60 GeV
$E_{\text{T}}^{\text{miss}}$	≥ 250 GeV

jets to reconstruct the VLQ candidates. Figure 20 shows a schematic of the VLQ decays and how the algorithm combines the objects.

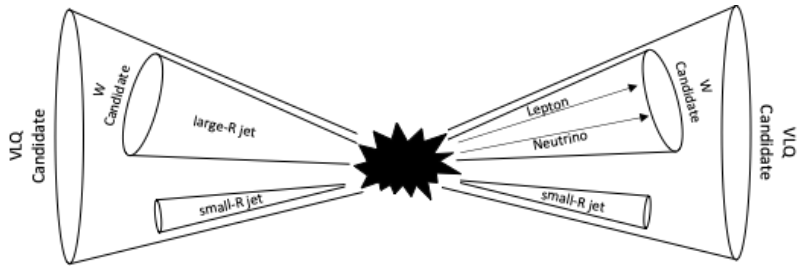

Figure 20: Schematic showing how the VLQ candidates are reconstructed. The W-boson candidates are reconstructed with the large-R jets and the lepton with a reconstructed neutrino. The VLQ candidates are reconsturcted with the W-boson candidates and the small-R jets.

Hadronically Decaying W-boson Candidate: The W-tagging algorithm provided by the ATLAS collaboration identifies large-R jets, which are likely to be the result of a hadronically decaying W boson. If this algorithm tags at least one large-R jet, the leading large-R jet is the W boson candidate. If no jet is tagged by the W-tagger, the large-R jet with a mass closest to the mass of the W boson (80.38 GeV) is the W boson candidate.

Neutrino Reconstruction: This analysis assumes that the $E_{\text{T}}^{\text{miss}}$ in each event results from only one neutrino. This assumption means that the p_{X} and p_{Y} of the neutrino can be calculated directly from the $E_{\text{T}}^{\text{miss}}$ of the event. The p_{Z} must be calculated to reconstruct the neutrino fully. A constraint is used that adding the four-momentum of the lepton and neutrino results in the four-momentum of the leptonically decaying W boson. From special relativity, the square of a W boson's four-momentum must equal the squared mass of the W boson. This constraint allows for the p_{Z} of the neutrino to be calculated.

Leptonically Decaying W-boson Candidate: The leptonically decaying W-boson candidate is the addition of the lepton and the reconstructed neutrino.

VLQ Candidates: The W bosons are combined with a small-R jet to reconstruct the VLQ candidates. The VLQ candidates have the same mass since the search is for the pair production of the same particle. The VLQ candidates are the combination that results in the smallest mass difference. The reconstruction algorithm only uses the three leading small-R jets since the quarks from the VLQ decay are boosted.

4.3.4 Signal Regions

The signal regions underwent optimization to ensure that they were sensitive to the kinematics of the signal process. Variables that separate SM processes and the signal create the selections for the regions. The value for each variable is the one which maximized the number of signal events and the simple significance $\left(N_{\text{signal}}/\sqrt{N_{\text{SM}}}\right)$. Figure 21 shows the optimization on the S_{T} variable. the S_{T} is defined as the scalar sum of $E_{\text{T}}^{\text{miss}}$, the lepton the p_{T}, and the p_{T} of every small-R jet. The ratio in the left plot is the addition of the SM events and the signal events divided by the SM events showing that the signal is at S_{T} while the SM events are at lower values. The plot on the right shows the number of signal events vs. the simple significance for different S_{T} cuts.

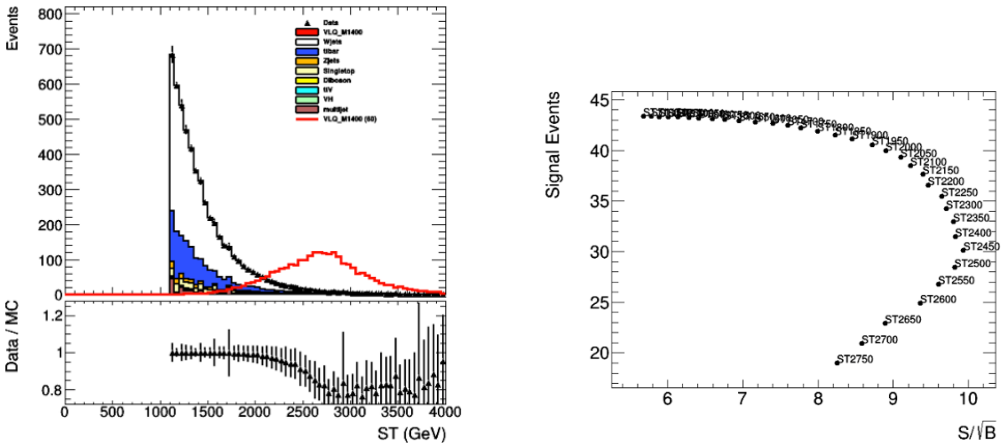

Figure 21: The S_{T} distribution (left) shows that signal is centered around a high value than the SM events. This shows that this kinematic variable is a good choice to define the signal region. The number of signal events vs the simple significance distribution (right) shows that a selection requirement of 2000 GeV does not remove too many signal events while also increases the sensitivity.

The signal process has no bottom quarks in the final state since this analysis searches for VLQs decaying to light quarks. The ATLAS collaboration provides a b-tagging algorithm identifying small-R jets likely to have been created from a bottom quark. The signal regions for this analysis require all small-R jets in the event to not be b-tagged. The regions also require the large-R jet to be W-tagged to increase the

likeliness that the jet did originate from a hadronically decaying W boson. The large momentum of the W bosons from the decay of the VLQ will result in a collimated lepton and neutrino, so a cut is applied that requires the azimuthal angle between the lepton and the $E_{\mathrm{T}}^{\mathrm{miss}}$ is at most 0.5. A selection on the angular distance of at least 0.8 had a good separation between SM events and signal. With every object being boosted from the large mass of the VLQs, a cut on the S_{T} of at least 2000 GeV was added. The final selection split created two separate signal regions. This selection requires that the angular distance between the leading small-R jet and the $E_{\mathrm{T}}^{\mathrm{miss}}$ is less than 2.75 for the first signal region and at least 2.75 for the second. Table 4 summarizes the selections for the signal regions.

Table 4: Summary of the selections used to define the signal regions.

Signal Region 1 (2)	
Variable	Cut
$N_{\text{b-tags}}$	$== 0$
$N_{\text{W-tags}}$	≥ 0
$\Delta\Phi$(lep, $E_{\mathrm{T}}^{\mathrm{miss}}$)	≤ 0.5
Δ R(had W, lep W)	≥ 0.8
S_{T}	≥ 2000 GeV
$\Delta\Phi$(lead jet, $E_{\mathrm{T}}^{\mathrm{miss}}$)	< 2.75 (≥ 2.75)

4.4 Background Modeling

The contribution from SM processes is estimated using MC. However, MC can mis-model some of the kinematic distributions for processes resulting in a disagreement when comparing data and MC. A data-driven correction is applied to the MC to fix any mis-modeling. The W+Jets, $t\bar{t}$, single top, and multijet MC all receive a correction for this analysis.

Nine regions are used to derive and check the corrections for the four MC estimations. Three CRs are where the corrections are derived, and five VRs check the data-to-MC agreement after the corrections. Each of these regions is orthogonal to each to each other and is orthogonal to the signal regions. The orthogonality is essential in the region definitions to ensure the corrections are not biased. Table 5 summarizes the selections for all regions.

Table 5: Table summarizing the definition of all the control and validation regions used in this analysis. The signal region (SR) definitions are also included to show the orthogonality of all the regions. Any seleciton not used in a region is left blank.

	SR1(2)	multijet CR	multijet VR	wjets CR	wjets VR1	wjets VR2	ttbar CR	ttbar VR1	ttbar VR2
$N_{\text{b-tags}}$	$== 0$	$== 0$	$== 0$	$== 0$	$== 0$	$== 0$	≥ 1	≥ 1	≥ 1
$N_{\text{W-tags}}$	≥ 1	$== 0$	≥ 1	$== 0$	$== 0$	≥ 1	≥ 1	$== 0$	$== 0$
$\Delta\Phi$(lep, $E_{\text{T}}^{\text{miss}}$)	≤ 0.5	≤ 0.1	≤ 0.1		> 0.1	> 0.1			
Δ R(had W, lep W)	≥ 0.8	< 0.8	< 0.8	≥ 0.8	< 0.8	< 0.8	< 0.8	< 0.8	≥ 0.8
S_{T}	≥ 2000GeV								
$\Delta\Phi$(lead jet, $E_{\text{T}}^{\text{miss}}$)	≤ 2.75								

4.4.1 Correction Calculations

An iterative process is used to calculate the corrections. The order of the MC corrections is multijet, then $t\bar{t}$ and single top, followed by W+Jets. Each correction is applied to the MC before deriving the correction for the following process. For example, the correction calculated for the multijet background is applied to the MC before deriving the correction for $t\bar{t}$ and single top. The process repeats once each process has a correction. When rederiving the correction for a process, the previous correction is not applied while the other MC have their latest correction used. For example, the correction for $t\bar{t}$ and single top is not applied on the second iteration, but the second iteration correction to multijet and the first iteration to W+Jets are. Table 6 summarizes the process.

Table 6: Process used to derive the corrections for MC mismodeling.

Step	MC being Corrected	Corrections being Applied
1	Multijet	-
2	$t\bar{t}$ and single top	1
3	W+Jets	1, 2
4	Multijet	2, 3
5	$t\bar{t}$ and single top	3, 4
6	W+Jets	4, 5

The process to calculate the correction is the same for each process. Every MC estimate is subtracted from the data if the MC is not the process being corrected. This subtraction results in an estimate of how much the process of interest is in the data. The ratio of the modified data and the process of interest gives how much the MC mis-models the data. Normalization correction uses the yields of the events, and the resulting ratio is applied to every event to correct the mis-modeling. If a shape correction is needed, the correction process uses a kinematic distribution. The resulting ratio distribution is fit with a function, and a weight is applied to events based on this fit.

4.4.2 Multijet Correction

Multijet is a subdominant process in this analysis. A jet must be misidentified as a lepton for an event to enter the signal region, making it difficult to estimate the

contribution of this process to the background accurately. A normalization correction adjusts the multijet estimation yield to estimate better the correct number of events with a misidentified jet. Figure 22 shows the data to multijet MC comparison before (left) and after (right) the correction.

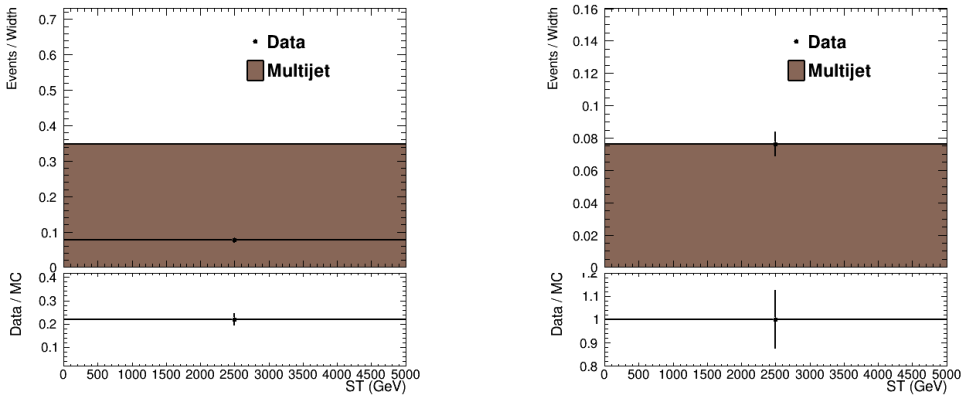

Figure 22: Figures showing the data to multijet comparisons. Before any correction is applied the multijet MC has a yield roughly one fourth of the data (left). The data and multijet MC have great agreement after the correction is applied to the MC (right).

4.4.3 $t\bar{t}$ Correction

$t\bar{t}$ is the second dominant background in the signal region. Previous analyses have found mis-modeling of p_{T} related variables in the $t\bar{t}$ MC. The shape correction uses the S_{T} variable to fix this mis-modeling. Due to similarities in the production of single top and $t\bar{t}$, the correction combines the signal top and $t\bar{t}$ estimation. Figure 23 shows the data to MC agree before (left) and after (right) the agreement. The ratio in the left distribution is fit with an exponential plus an offset $\left(P_0 + e^{P_1 x}\right)$ for the correction. The correction results in great agreement.

4.4.4 W+Jets Correction

W+Jets is the dominant background in the signal region. A shape correction is calculated to ensure that the modeling of this critical background is correct. The correction is a function of S_{T}, and the resulting ratio is fit with an exponential plus an offset $\left(P_0 + e^{P_1 x}\right)$. This variable and fit function were chosen to be consistent with the $t\bar{t}$ correction. Figure 24 shows the data to MC agree before (left) and after (right) the agreement. The correction results in excellent agreement.

4.4.5 Uncertainties to the Shape Corrections

Two separate shape uncertainties apply to the calculated corrections corresponding to the uncertainty related to the offset (P_0) and decay (P_1) parameters of the fits.

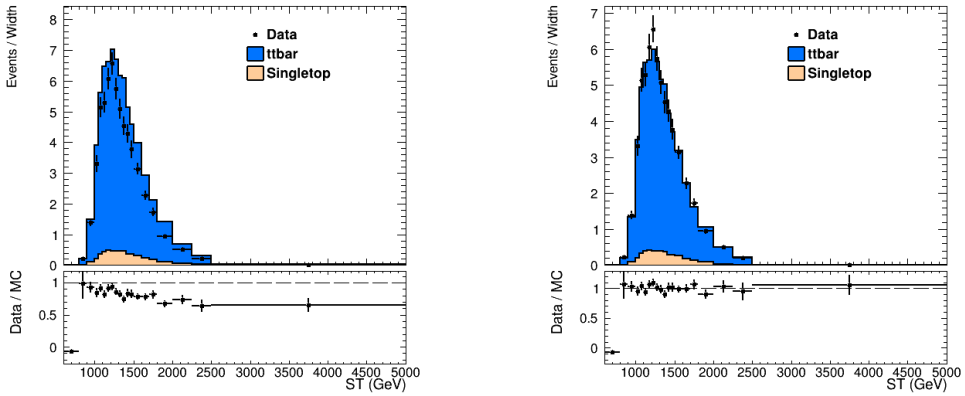

Figure 23: Figures showing the comparisons between data and the MC estimate of $t\bar{t}$ and single top. Before any correction is applied a difference is observed bewteen the MC and data (left). The data and MC have great agreement after the correction is applied to the MC (right).

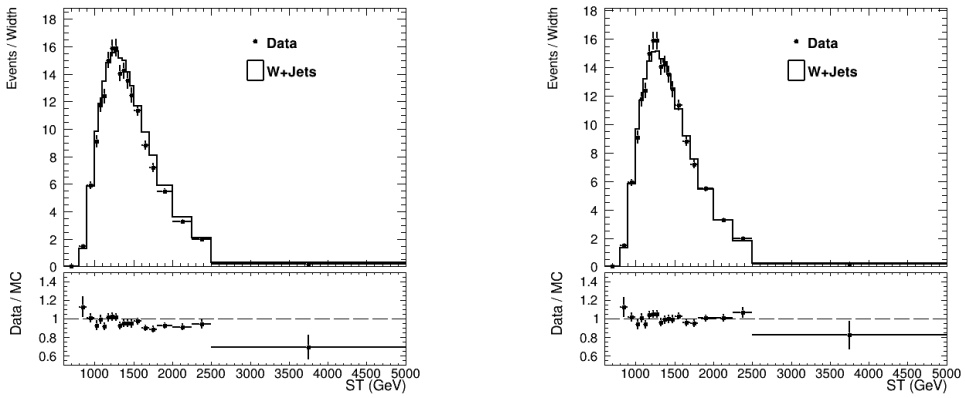

Figure 24: Figures showing the comparisons between data and the MC estimate of W+Jets. Before any correction is applied a difference is observed bewteen the MC and data (left). The data and MC have great agreement after the correction is applied to the MC (right).

Independent, alternate fits were found by using the eigenvectors $\left(\vec{X}_1 \text{and} \vec{X}_2\right)$ and eigenvalues $(\lambda_1 \text{and} \lambda_2)$ of the covariance matrix for the fit parameters. The parameters for the alternate fits are $P_0 \pm \left(\Delta P_0 \times \vec{X}_{1i} \times \sqrt{\lambda_1}\right)$ and $P_1 \pm \left(\Delta P_1 \times \vec{X}_{2i} \times \sqrt{\lambda_2}\right)$ where i = 1 or 2. Figure 25 shows the alternate fits used for the uncertainties for $t\bar{t}$ and single top (left) and W+Jets (right).

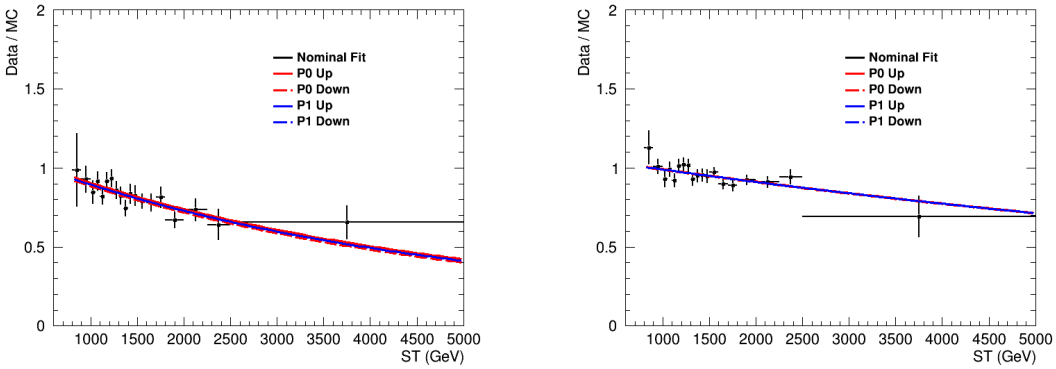

Figure 25: Figure showing the alternate fits used as the uncertainties for $t\bar{t}$ and single top (left) and W+Jets (right). The red lines correspond to the shape on the offset parameter (P0) and the blue line corresponds to the uncertainty on the decay parameter (P1).

4.4.6 Post Correction Agreement

VRs check the data-to-MC agreement after the corrections to the MC. The variables most important to check the modeling of are those used to define the signal region and the discriminating variable. All regions and variables had agreement post-correction, but only three variables in the ttbarVR2 and wjetsVR2 are presented since these regions are the two which are kinematically closest to the signal regions. The variables shown are the angular distance between the W boson candidates, S_{T}, and $M_{\mathrm{VLQ}}^{\mathrm{lep}}$. These variables show the modeling of angular variables, p_{T} related variables, and the discriminating variable.

Monte Carlo Agreement ttbarVR2

Figure 26 shows the data-to-MC comparison before (top row) and after (bottom row) the corrections in the ttbarVR2. The distributions also show the total uncertainty with the shaded region. The ratio for the pre-correction distributions indicates clear mis-modeling since the ratio is not at one. Post-correction, the ratio moves closer to one, no trend is in the ratio, and all points are within the uncertainty showing the correction fixed the mis-modeling.

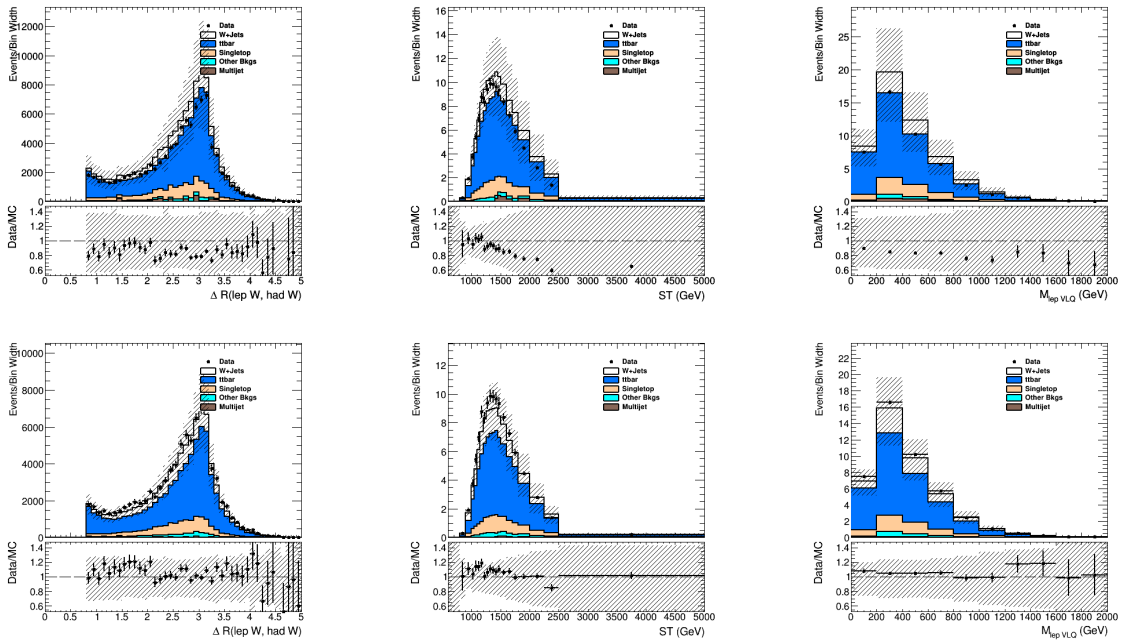

Figure 26: Distributions showing the data to MC comparisons before any corrections applied (top row) and after the correctons are applied (bottom row). The distributions are the radial distance between the W-boson candidates (left) to check angular modeling, S_{T} (middle) to check the momentum modeling, and the mass of the leptonically decaying VLQ (right) to check the modeling of the discriminating variable. The corrections to the MC results in good agreement.

Monte Carlo Agreement wjetsVR2

Figure 27 shows the data-to-MC comparison before (top row) and after (bottom row) the corrections in the ttbarVR2. The distributions also show the total uncertainty with the shaded region. The ratio for the pre-correction distributions indicates clear mis-modeling since the ratio is not at one. Post-correction, the ratio moves closer to one, no trend is in the ratio, and all points are within the uncertainty showing the correction fixed the mis-modeling.

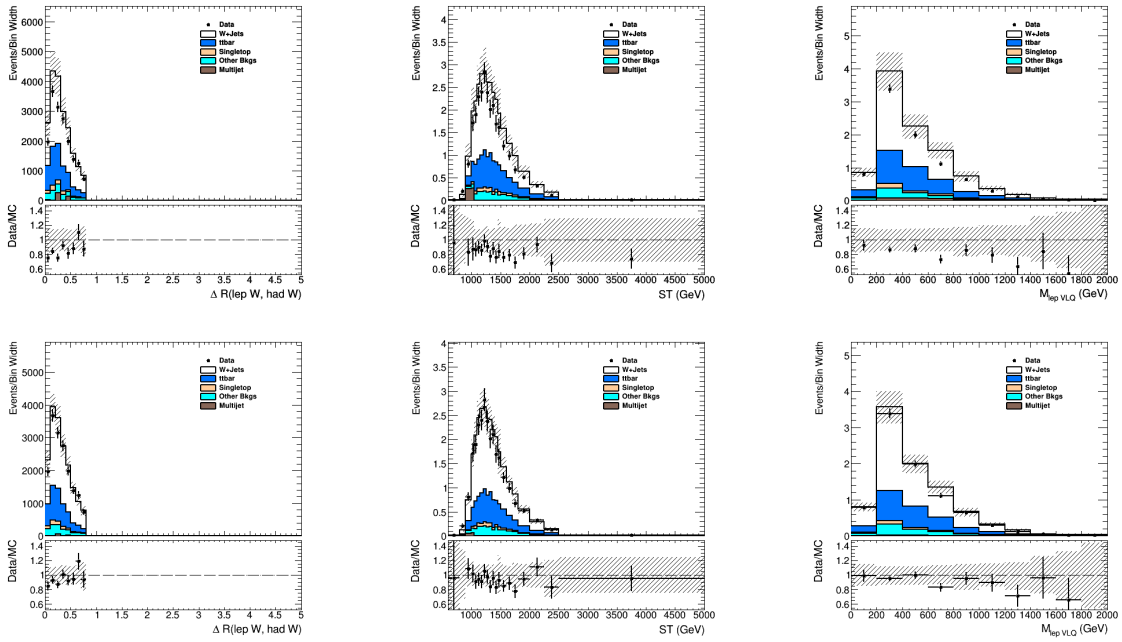

Figure 27: Distributions showing the data to MC comparisons before any corrections applied (top row) and after the correctons are applied (bottom row). The distributions are the radial distance between the W-boson candidates (left) to check angular modeling, S_{T} (middle) to check the momentum modeling, and the mass of the leptonically decaying VLQ (right) to check the modeling of the discriminating variable. The corrections to the MC results in good agreement.

Residual Uncertainty

When checking the modeling in the wjetsCR after the correction, the discriminating variable still had mis-modeling. W+Jets get an extra uncertainty to account for this mis-modeling. The additional uncertainty is a straight-line fit to the post-correction ratio. Figure 28 shows the post-correction data-to-MC agreement (left) and the effect of the additional uncertainty on the discriminating variable (right).

4.5 Systematic Uncertainties

Systematic uncertainties in this analysis fall into experiment and theoretical uncertainties. The experimental uncertainties are related to calibration factors, detector

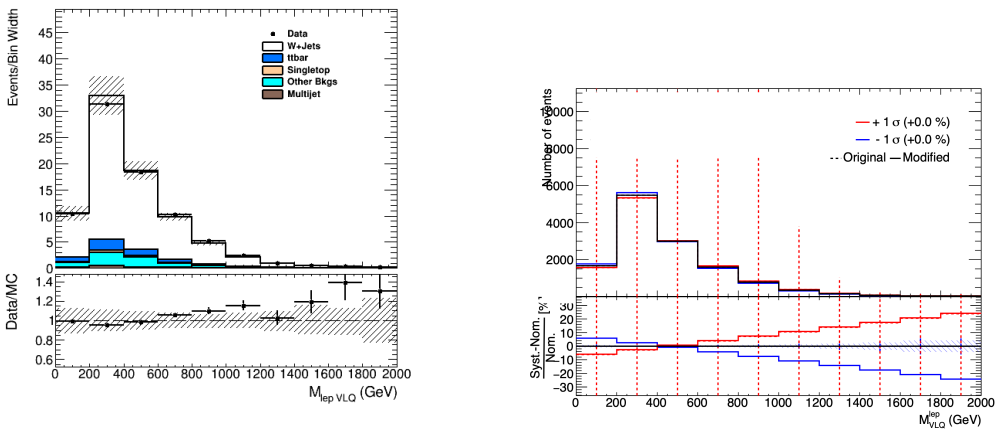

Figure 28: Comparison of data and MC in the wjetsCR after the corrections for the mass of the leptonically decaying VLQ distribution (left). A trend is still seen in the ratio so an extra uncertainty is added to account this behavior. The uncertainty includes an up and down variation which is equivalent to the slope seen in the ratio (right).

response, and object reconstruction. Theoretical uncertainties pertain to modeling the physics used in the MC simulation and mis-modeling corrections.

4.6 Statistical Analysis

The discriminating variable, $M_{\mathrm{VLQ}}^{\mathrm{lep}}$, is used in a binned likelihood fit between the data and MC to determine the presence of the signal process. The fit is done simultaneously in the two signal regions. Every uncertainty for the MC is a nuisance parameter the fit can pull to maximize the likelihood between the data and the MC estimate. The fit also scales the signal distribution (signal strength). Figure 29 shows the discriminating variable in the two signal regions before (top row) and after (bottom row) the fit for a VLQ with a mass of 1400 GeV. The post-fit results in excellent agreement between data and MC since all the ratio points are within the uncertainty. The nominal signal strength for this fit is zero, but the fit determines the maximum signal strength allowed such that the data would agree with the background plus signal 5% of the time. The cross-section needed to produce this many signal events equals this signal strength multiplied by the theoretical cross-section. The statistical analysis results give two experimentally determined cross-sections. The first is if the data matches the SM background (Asimov data), called the expected cross-section. The other result is the observed cross-section which is the result from the data.

4.7 Results

The statistical analysis calculates the expected and observed cross-sections as a function of the mass of the VLQs by performing the fit multiple times with signal MC for each mass. The data is determined to be consistent with the SM-only hypothesis if the observed and expected cross-sections are equal. If this is the case, any mass with

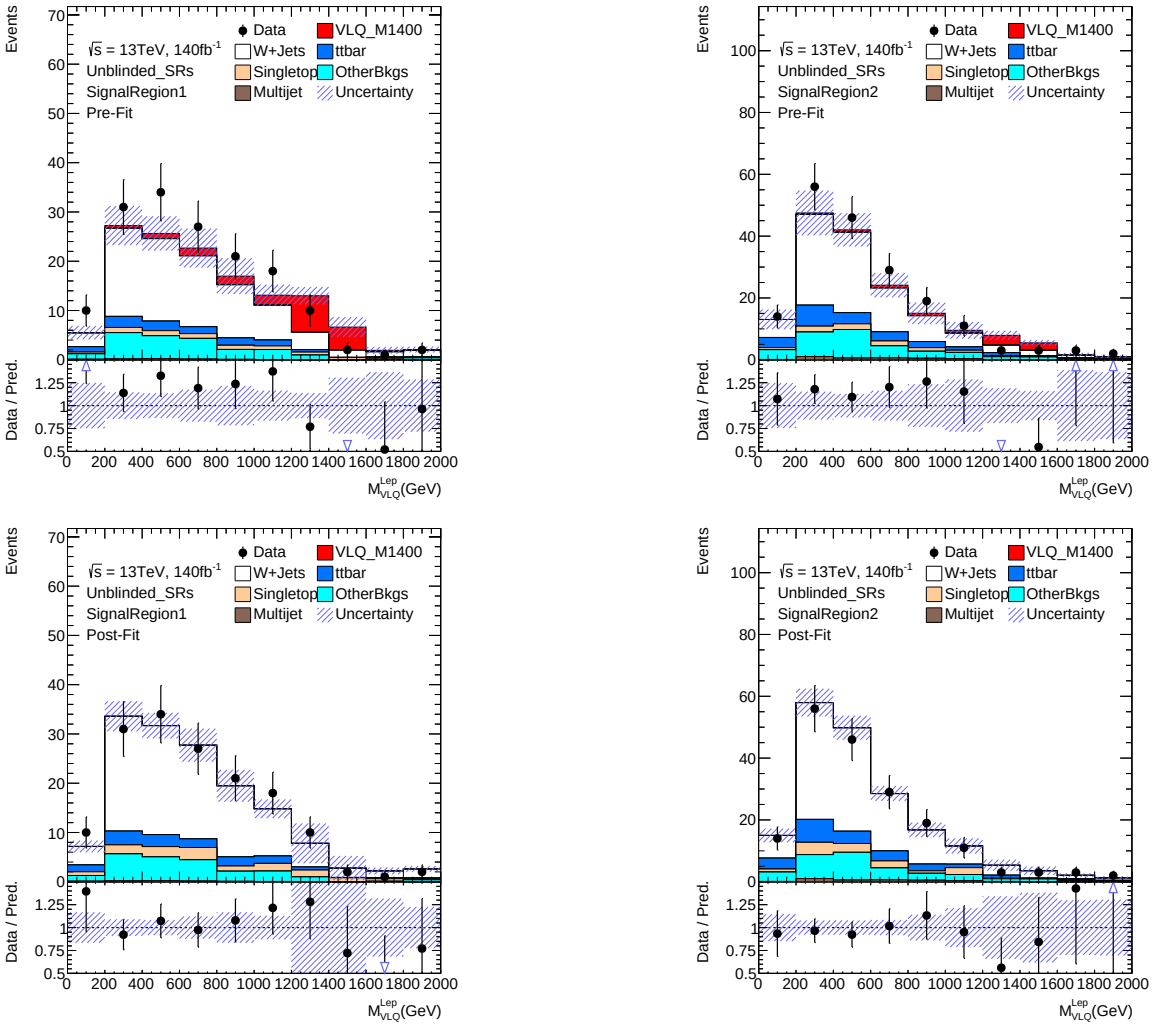

Figure 29: The discriminating variable before (top) and after (bottom) the fit. The left side shows the variable in SR1 and the right shows SR2. The post-fit data-to-MC agrrement is all within uncertainties showing good agreement.

an observed cross-section less than the theoretical cross-section is excluded at a 95% confidence level since the maximum production of the signal is inconsistent with the theory. Figure 30 shows the expected, observed, and theoretical cross-section from the statistical analysis. Comparing the expected and observed cross-sections shows the data is consistent with the SM-only hypothesis since the values never deviate more than 1 σ from each other. Comparing the observed and theoretical cross-sections shows the lowest allowed mass of the VLQs decaying to a W boson and light quark has increased from the 800 GeV set in the previous run of the analysis to 1550 GeV.

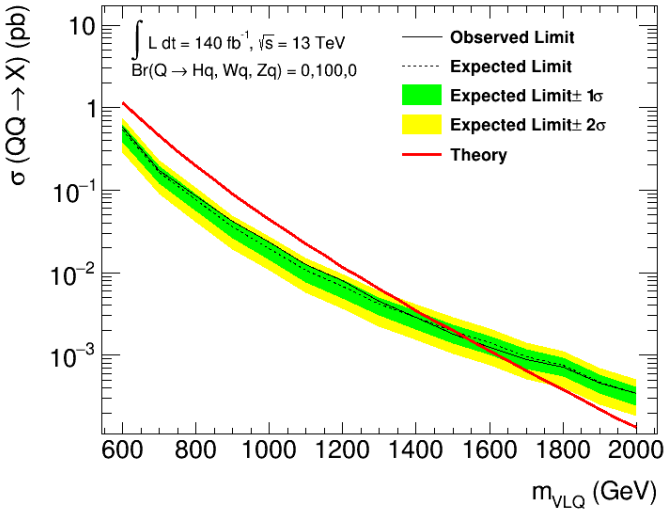

Figure 30: Figure showing the observed and expected 95% confidence level upper limits on the cross-section as a function of the mass of the VLQ. This limit is for a branching ratio of 100% to a W boson and light quark.

This analysis was most sensitive to looking for VLQs which decay 100% of the time to a W boson and light quark. However, VLQs are not required to decay through a W boson. Many theories of VLQs have the decay through all three SM bosons with different percentages. The branching ratios (BRs) specify the fraction of VLQs which will decay through a given channel. For example, if a theory states that the BR for the W channel is 0.5, this means that 50% of the time, the VLQ will decay to a W boson and light quark. The only constraint is the sum of all three BRs must equal one.

The final step of the analysis is to scan all possible BRs for the VLQ decay. Different signal MC samples are created for each BR combination and are in the statistical analysis. Figure 31 shows the lower mass bound for the VLQ for a given BR. The X-axis is the BR through the W boson, the Y-axis is the BR through the Higgs boson, and the color is the lower mass bound. Any white point is forbidden since the sum of the BRs would be greater than 1.

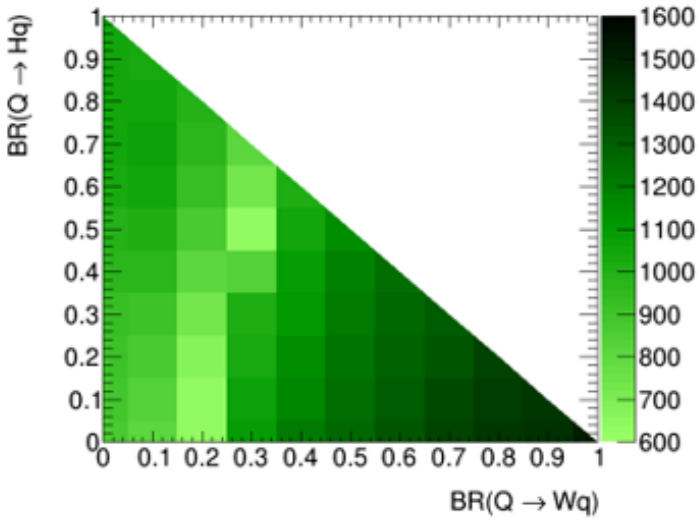

Figure 31: Plot showing the lowest mass not excluded for all possible decays of VLQs. The X-axis shows the BR for decaying to a W boson, the Y-axis is the BR for decaying to a Higgs boson, and the color is the lowest mass not excluded for the BR combination.

CHAPTER V

Wb+X Analysis

This chapter discusses an analysis searching for the pair production of vector-like quark (VLQ) partners to SM top (t) quark decaying to the semi-leptonic Wb+X final state. This analysis is optimized for both VLQs to decay to a W boson and b-quark, but one W boson must decay leptonically while the other decays hadronically. Figure 32 shows the Feynman diagram for this analysis.

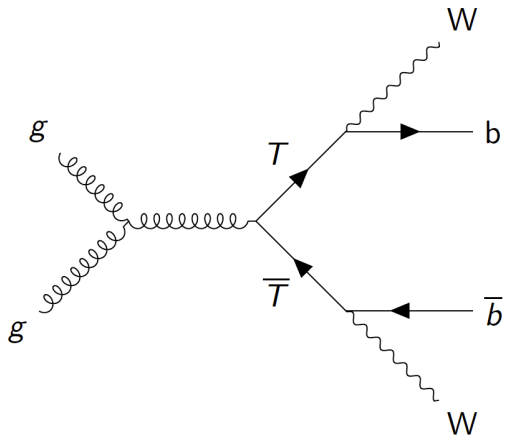

Figure 32: Feynamn diagram of the signal for this analysis.

5.1 Analysis Strategy

This analysis is similar to the search presented in Chapter IV except the light quarks from the VLQ decays are b-quarks. This difference changes the dominant SM process from W+Jets to $t\bar{t}$. This analysis's main steps are the same as Wq+X so this chapter will focus on the differences.

5.2 Monte Carlo Simulation

The background processes used in this analysis are all the same except for one. The presence of the b-quarks from the VLQ decay makes subdominant processes that produce a t-quark more critical than those with a Z or W boson, so rare tops are used instead of VH. The processes in this analysis are:

- W+Jets: Production of a leptonically decaying W-boson and extra jets

- $t\bar{t}$: Pair production of SM top quarks decaying with at least one lepton
- Single top: Production of one SM top quark
- Z+Jets: Production of a leptonically decaying W-boson and extra jets
- ttV: Pair production of SM top quarks along with a vector boson (W or Z)
- Disboson: Production of two vector bosons
- Rare tops: Rare processes which produce a SM tops
- Multijet: Collision creating nothing but jets
- VLQ Signal: Pair production of vector-like quarks

A small number of events from Z+Jets, ttV, diboson, and rare tops contribute to any region so they are combined into one process called "Other Bkgs". The specific details for the MC generation can be found in the publication for this analysis [25].

5.3 Event Selection

Events must pass a series of selections to ensure they are kinematically close to the signal process. The "primary selection" provides events with a similar final state, and "preselection" ensures enough physics objects to reconstruct two VLQ candidates. The events which pass these selections are sorted into CRs, VRs, and SRs.

5.3.1 Primary Selection

The decay of the VLQ results in events with a lepton and a large $E_{\mathrm{T}}^{\mathrm{miss}}$, so this analysis uses both single lepton and $E_{\mathrm{T}}^{\mathrm{miss}}$ triggers. The $E_{\mathrm{T}}^{\mathrm{miss}}$ trigger is fully efficient for events with a $E_{\mathrm{T}}^{\mathrm{miss}}$ greater than 200 GeV. The single lepton trigger is used for every event with a $E_{\mathrm{T}}^{\mathrm{miss}}$ below that threshold to try to increase the number of signal events.

Except for the presence of b-jets, the final state for this analysis of a lepton, $E_{\mathrm{T}}^{\mathrm{miss}}$, and jets is analogous to the Wq+X analysis described in Chapter IV. Thus the primary event selection is the same as for Wq+X, as shown in Table 7.

Table 7: Summary of the primary selection.

Primary Selection	
Variable	Cut
N_{lepton}	$== 1$
$p_{\mathrm{T}}^{\mathrm{el(mu)}}$	$\geq 27(25)$ GeV
$N_{\text{small-R jets}}$	≥ 3
$p_{\mathrm{T}}^{\text{small-R jets}}$	≥ 25 GeV

5.3.2 Preselection

The preselection for this analysis ensures that two VLQ candidates can be reconstructed. The selections are like those for Wq+X with less strict p_{T} requirement. The most significant difference is the b-quarks from the VLQ decays in this analysis. The ATLAS collaboration provides an algorithm that identifies small-R jets likely to have originated from a b-hadron [28]. This analysis requires that at least one small-R jet is b-tagged using the criteria corresponding to an efficiency of 77% [29]. Table 8 summarizes the preselection definition.

Table 8: Summary of the preselction requirements.

Preselection	
Variable	Cut
N_{leptons}	$== 1$
$p_{\mathrm{T}}^{\text{lepton}}$	≥ 25 GeV
$N_{\text{small-R jets}}$	≥ 3
$p_{\mathrm{T}}^{\text{small-R jets}}$	> 20 GeV
$N_{\text{b-tagged jets}}$	≥ 1
$E_{\mathrm{T}}^{\text{miss}}$	≥ 60 GeV

5.3.3 Reconstuction of VLQ Candidates

Any event that passes the preselection goes through an algorithm to reconstruct two VLQ candidates. The leptonically decaying W boson is reconstructed by combining the lepton in the event with a reconstructed neutrino. The neutrino reconstruction is explained in the Wq+X analysis Chapter 4.3.3. The hadronically decaying W boson candidate is the W-tagged large-R jet with a mass closest to the W boson.

The VLQ candidates are reconstructed by combining the W bosons with the small-R jets to minimize the mass difference between the reconstructed VLQ. If there is only one b-tagged small-R jet in the event, that jet is used, and every combination with the other small-R jets is tested. Otherwise, the two-leading b-tagged small-R jets are used in the reconstruction. Figure 33 is a schematic of how the VLQ reconstruction is performed.

5.3.4 Signal Regions

This analysis has two signal regions (SR1 and SR2) based on the quality of the reconstructed VLQ candidates. Since the same particle is created, the mass difference between two good reconstructed VLQ candidates (ΔM_{VLQ}) will be low. SR1 in this analysis requires that ΔM_{VLQ} is less than 200 GeV. This selection results in a

discriminating variable $\left(M_{\mathrm{VLQ}}^{\mathrm{lep}}\right)$ that is a sharp, narrow peak at the mass of the VLQ for signal and an exponential decay shape for the SM processes. SR2 requires the ΔM_{VLQ} to be at least 200 GeV but less than 500 GeV. The higher ΔM_{VLQ} gives the signal a broader peak in the discriminating variable, but there is still separation from the SM processes.

The rest of the selections for the signal regions take advantage of the large mass of the VLQ. Variables that had a good separation between SM and signal underwent an optimization study to find a value for the cut that would be the best. Chapter 4.3.4 details how the optimization is performed. Table 9 summarizes the signal region definitions.

Table 9: Summary of the selections used to define the signal regions.

SR1 (SR2)	
Variable	Cut
$p_{\mathrm{T}}^{\mathrm{el}}$	> 60 GeV
$N_{\text{W-tag}}$	≥ 1
$\Delta R(\text{lep}, \nu)$	< 0.7
S_{T}	> 1.9 TeV
$\Delta R(\text{W-tag, b-tag})$	> 1.0
$\Delta M_{\mathrm{VLQ}}^{\mathrm{SR1}}$	200 GeV
$\Delta M_{\mathrm{VLQ}}^{\mathrm{SR2}}$	200→500 GeV

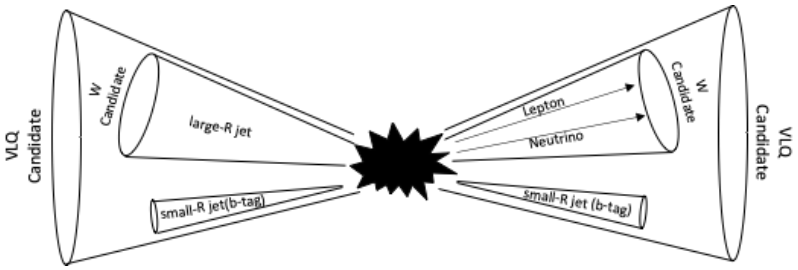

Figure 33: Schematic showing how the VLQ candidates are reconstructed. The W-boson candidates are reconstructed with the large-R jets and the lepton with a reconstructed neutrino. The VLQ candidates are reconsturcted with the W-boson candidates and the small-R jets where at least one is b-tagged.

5.4 Background Modeling

The contribution from SM processes is estimated using MC. However, MC can mis-model some of the kinematic distributions for processes resulting in a disagreement when comparing data and MC. A data-driven correction is applied to the MC to fix any mis-modeling. The W+Jets, $t\bar{t}$, single top MC all receive a correction for this analysis.

5.4.1 W+Jets Correction

The b-tag requirement in the signal region makes W+Jets the second-largest background, so only a normalization correction is applied to the MC estimate. The correction for W+Jets is calculated in the W+Jets CR. A b-tag is required for each event to keep the CR kinematically close to the signal region. A consequence of requiring a b-tag is that $t\bar{t}$ will tend to dominate the region. Other selections are made to reduce the number of $t\bar{t}$ events. Table 10 summarizes the W+Jets CR definition.

Table 10: Summary of the selections used to define the W+Jets control region.

W+Jets Control Region	
Variable	Cut
$N_{\text{b-tagged jets}}$	≥ 1
$p_{\text{T}}^{\text{lep}}$	> 40 GeV
S_{T}	> 1.9 TeV
$\Delta R(\text{lep}, \nu)$	< 1.0
$N_{\text{large-R jets}}$	≥ 1
$N_{\text{modified W-tags}}$	≥ 1

The charge-asymmetry variable is used to calculate the normalization correction for W+jets. Charge-asymmetry equals the difference between the number of events with a positive lepton and the number of events with a negative lepton. The charge-asymmetry equals zero for charge-symmetric processes, such as $t\bar{t}$. The normalization correction for W+Jets is the charge asymmetry of the data divided by the charge asymmetry of the MC. Additional uncertainties are applied to this normalization to account for other charge asymmetric processes, such as the single top background. This procedure results in a correction of 0.95 to the W+Jets MC.

5.4.2 $t\bar{t}$ Correction

$t\bar{t}$ is the dominant background in the signal regions. A shape correction is calculated for $t\bar{t}$ since previous analyses have observed mis-modeling. The final state of $t\bar{t}$ is the

same as the signal process, except the mass of the SM top is less than the lowest non-excluded VLQ mass. The $t\bar{t}$ control region is the same as the signal region with some exceptions to account for the difference in mass. To make this region orthogonal to the signal regions, the mass of the reconstructed leptonically decaying VLQ candidate must be less than 700 GeV, almost half the lowest allowed mass of the VLQ. Table 11 summarizes the $t\bar{t}$ control region definition.

Table 11: Summary of the selections used to define the $t\bar{t}$ control region.

$t\bar{t}$ Control Region	
Variable	Cut
$N_{\text{b-tags}}$	≥ 2
$\Delta R(\text{lep}, \nu)$	< 1.2
S_{T}	> 800 GeV
$N_{\text{W-tag}}$	≥ 1
$\Delta R(\text{W-tag}, \text{b-tag})$	< 1.0
M_{VLQ}	< 700 GeV

The shape correction is calculated as a function of S_{T} since $t\bar{t}$ is known to have some mis-modeling in p_{T} related variables. The correction procedure starts by subtracting the MC not being corrected from the data. The modified data and the $t\bar{t}$ plus single top MC are normalized to remove normalization differences in the distributions. The ratio of the normalized distributions is fit, and this function is used to calculate weights for each MC event. Figure 34 shows the data-to-MC agreement before (left) and after (right) the shape correction. The correction leads to excellent agreement between data and MC.

5.5 Systematic Uncertainties

Systematic uncertainties in this analysis fall into experiment and theoretical uncertainties. The experimental uncertainties are related to calibration factors, detector response, and object reconstruction. Theoretical uncertainties pertain to modeling the physics used in the MC simulation and mis-modeling corrections.

5.6 Statistical Analysis

A binned likelihood fit is preformed between the data and MC using the discriminating variable. This analysis simultaneously fits the discriminating variable in five regions, three control regions, and two signal regions. The three control regions constrain parameters and extrapolate the constraints to higher S_{T}. This analysis is still blinded,

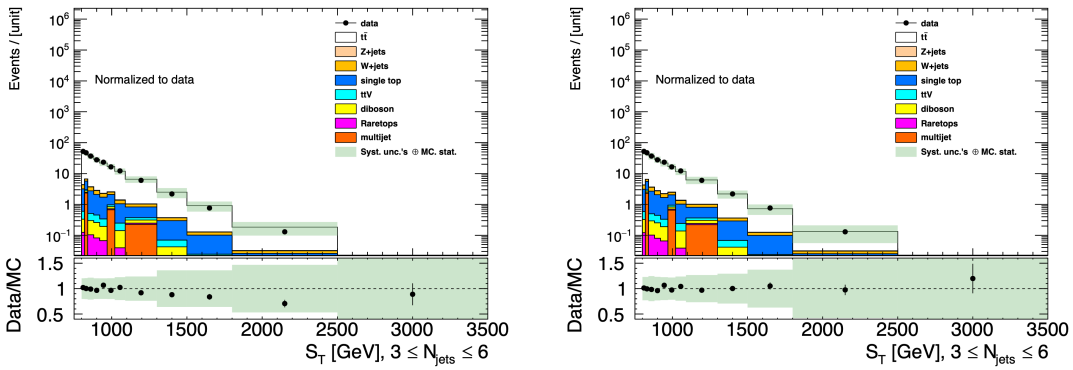

Figure 34: Plots showing the data-to-MC agreement before (left) and after (right) the shape correction. The correction leads to excellent agreement between data and MC.

so data cannot be observed in the signal region, so data collected by the ATLAS detector is replaced with Asimov data. Asimov data is created by summing together all the SM estimations. Figure 35 shows the post fit results in the control regions, the resulting Asimov data in the signal regions, and the region map to remember how each region is related.

Using Asimov data in the statistical analysis results in the sensitivity of the analysis if the data is consistent with the SM. The maximum signal strength is calculated so that the Asimov data would agree 5% of the time with the MC plus signal distributions. The cross-section uppler limit equals the signal strength multiplied by the theoretical cross-section.

5.7 Results

The fit is preformed for different masses of VLQ ranging from 1000 GeV to 2000 GeV in steps of 100 GeV. If the theoretical cross-section is greater than the experimentally calcuated cross-section, that mass is excluded. The point at which the two cross-sections equal each other is the expected sensitivity of the analysis. Figure 36 shows the theoretical and expected cross-sections as a function of mass. The expected sensitivity for the analysis is at 1550 GeV for the assumption that the branching ratio is 100% to W boson and b-quark.

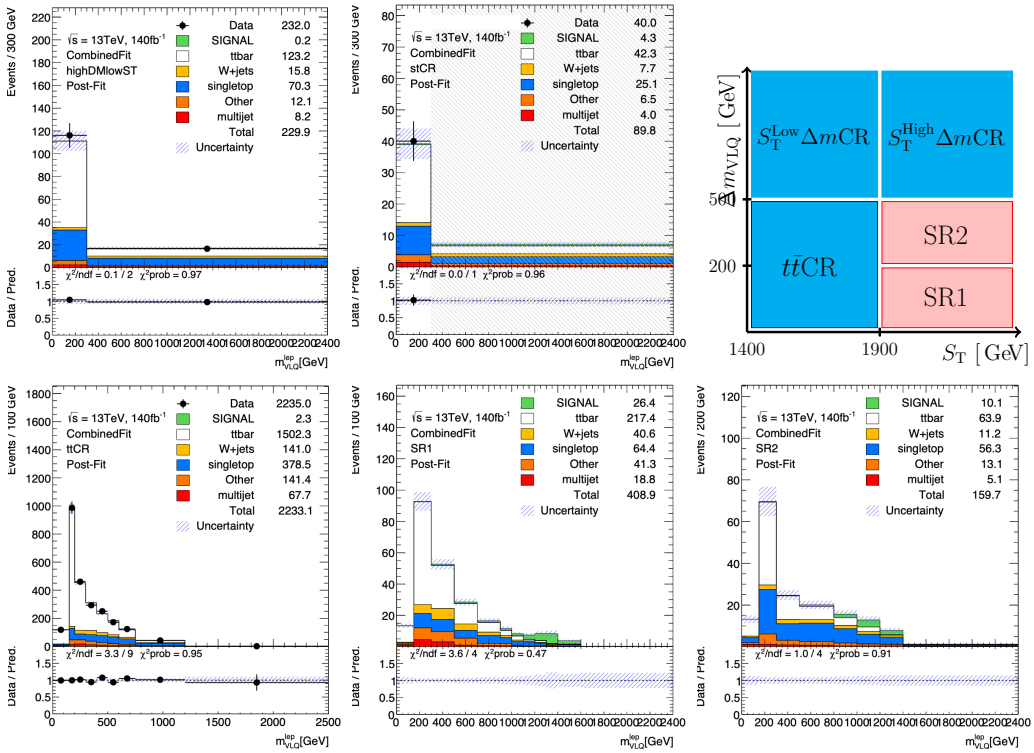

Figure 35: Illustration of the two-dimensional plane in S_{T} and Δm_{VLQ} on which the fit regions are defined and the post-fit distribution for the discriminating variable in each region.

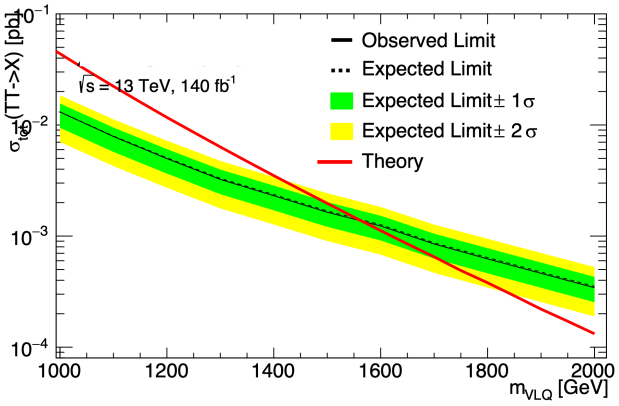

Figure 36: Figure showing the expected cross-sections of the VLQ as a function of the mass of the VLQ. This analysis is expected to be sensitive to VLQs up to a mass of 1550 GeV.

CHAPTER VI

The ATLAS Detector Inner Tracker Upgrade

At the beginning of 2026, the LHC powers down for three years for the Long Shutdown 3 to be upgraded to the High Luminosity LHC (HL-LHC) [15]. The HL-LHC aims to increase the integrated luminosity to 250 fb^{-1} each year with a total integrated luminosity of 3000 fb^{-1} in the 12 years of a planned operation. The main upgrades are the insertion regions to the ATLAS and CMS experiments, so the number of collisions per bunch crossing will be increased from 27 to 130.

During this time, the ATLAS detector will undergo an upgrade as well. One major upgrade to the ATLAS detector is replacing the current Inner Detector with the all-silicon Inner Tracker (ITk). The ITk system will have two subsystems, a pixel detector, and a strip detector. The pixel detector is the closest system to the collision point and covers an area of 13 m^2 around the beam pipe. The strip detector will surround the pixel detector and cover a total area of 160 m^2. Figure 37 shows the structure of the ITk where the blue lines show the strip detector layout and the red lines show the pixel detectors.

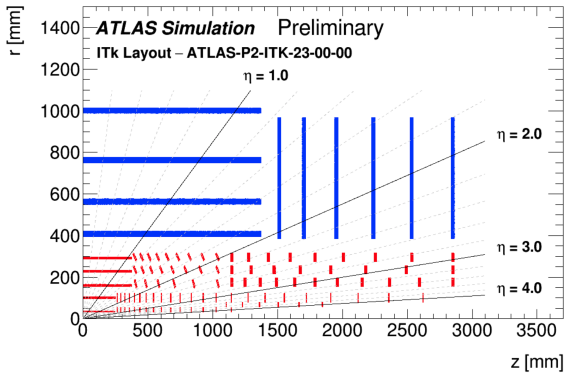

Figure 37: Schematic of the Inner Tracker layout. The layout of the pixel detector is shown in red, and the strip detector is shown in blue.

The pixel detector of the ITk, shown in Figure 38, has two independent systems, split by radial distance from the beam pipe. The Inner System (IS) consists of the two innermost layers of the detector, and the Outer System consists of the rest. These systems have two regions defined by the location on the Z-axis. The barrel region spans from 0 to 250 mm, represented by the horizontal lines, and the endcaps span from 250 to 3000 mm, represented by vertical lines. The prototypes created as work for this thesis were the Type-0 services for IS endcaps.

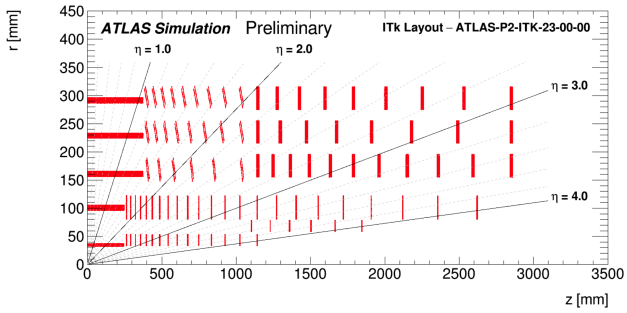

Figure 38: Schematic of the ITk pixel detector layout. The detector comprises the Inner System (two innermost layers) and the Outer System. Each system has a barrel region (horizontal lines) and endcaps (vertical lines).

6.1 Type-0 Services

The readout chain for the IS is comprised of services and patch panels. The data collected by the pixel sensors transmit the data to the Type-0 services. These services connect to Patch Panel 0 (PP0), which sends the data to the Type-1 services. This pattern repeats until the data reaches the readout.

The Type-0 services in the IS endcaps have three separate parts. The first part is the data pigtail which directly connects a pixel model. Multiple data pigtails connect to the Rigid Rings. The final component of the endcap is the Type-0 to PP0 flex. This component connects the Rigid Ring to the PP0. In the endcaps, the pixel modules and Type-0 services are within a carbon fiber shell which the PP0 sits on top of. The Type-0 to PP0 flex is a flexible PCB that bends through a hole in the carbon fiber shell. Figure 39 shows a rendering of one of the endcaps. The green pixel modules connect directly to the light brown data pigtails. These data pigtails connect to the Rigid Ring, which was made invisible in this rendering to show the modules the Rigid Ring mounts on top of. The red Type-0 to PP0 connects the Rigid Ring to the blue PP0 by bending through a hole in the translucent carbon fiber shell.

6.2 Prototype Designs

The Rigid Ring and Type-0 to PP0 flex were the PCBs designed for the prototype. The main emphasis for this prototype was to check the signal integrity of the data readout. Coplanar differential pairs transmit the data and command lines within the readout system. Differential pairs are two lines that carry the same signal, but one signal is inverted compared to the other. The final signal the DAQ uses is the difference between the inverted signals. Coplanar differential pairs have a ground line placed on either side of the differential pair. These ground lines ensure the differential pairs are isolated and do not receive interference from neighboring signals.

6.2.1 Rigid Ring Prototype

The Rigid Ring connects to both quad and triplet pixel modules. Quad modules contain four separate silicon pixel sensors, while the triplet modules have three. Each

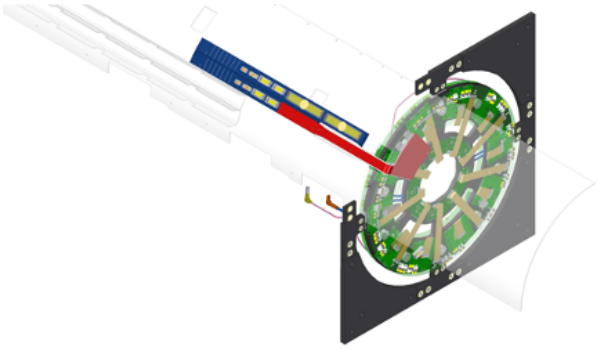

Figure 39: 3D model of one of the pixel detector endcaps. The pixel modules (green) connect to the data pigtails (light brown). The data pigtail connects to the Rigid Ring (invisible). The Rigid Ring is connected to the PP0 (blue) via the Type-0 to PP0 flex (red).

quad module needs five differential pairs for data and command, and the triplet modules require ten. The Rigid Ring connects to ten quad modules and three triplet modules. The modules are spaced evenly around the ring, and the data goes to two connectors connecting to the Type-0 to PP0 flex. Figure 40 shows the location of the connectors on the top of the PCB. The white square connectors are what the data pigtails plug into. The inner ring of connectors is for the quad modules, and the outer ring is for the triplet modules. The two large grey connectors connect the Rigid Ring to the Type-0 to PP0. All other connectors are only there for the prototype to allow easy access to check different quantities during tests.

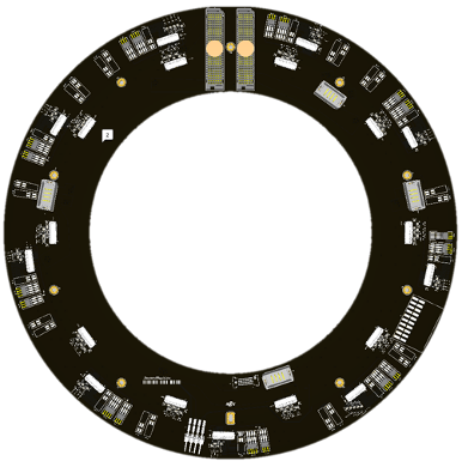

Figure 40: 3D model of the Rigid Ring. The data pigtails plug into the white connectors around the Ring. The data is transmitted from the white connectors to the grey rectangular connectors. All other connectors are to test different quantities during tests and will not be in the final design.

Copper traces are routed inside the board to transmit the data from the data pigtails to the Type-0 to PP0 flex. Two separate layers were required to route all the

differential pairs for the Rigid Ring. Figure 41 shows the copper routed within the Rigid Ring. The yellow traces (left) are the triplet modules' differential pairs, and the purple traces (right) are the traces for the quad modules.

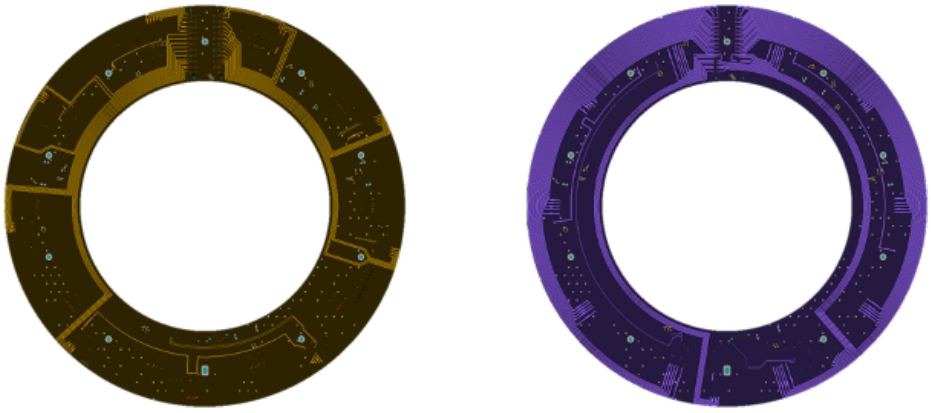

Figure 41: Picture of the data differential pairs in the Rigid Ring. The data for the triplet modules (left) and quad modules (right) are on separate layers of the Ring.

6.2.2 Type-0 to PP0 Flex Prototype

Two separate Type-0 to PP0 flexes were created for the prototype, one for each connector on the Rigid Ring. Each PCB carried the data for five quads, but one PCB transmitted the data for two triplets while the other transmitted one. The most significant constraint for these boards was the width at the PP0 end could be no more than 18 mm wide because the PP0 sits within an 18 mm wide channel. Figure 42 shows the routing of the differential pairs at the PP0 connector. Unlike the Rigid Ring, the layers do not represent the different pixel modules.

Figure 42: Picture of the data differential pairs in the Type-0 to PP0 flex at the PP0 connector. This area is the most significant constraint in designing the PCB. All data was still able to be routed on two layers.

6.3 Concept Design

In the next round of designs for the Rigid Ring, the Type-0 to PP0 flex connector will be changed. The mounting height of the current connector is too high to fit in the detector requiring a new connector to be used. This new connector has a lower mounting height and more pins. The increase in pins on the connector allowed for more data on each connector. There was enough added data per connector to create a common interface between the Rigid Ring and the Type-0 to PP0 flex. Previously, a different Type-0 to PP0 flex was required for every variation in the Rigid Ring. Not only was work done to create the interface, but a concept board was also created to show that the routing for the Type-0 to PP0 flex was possible. The creation of the common interface can drastically reduce the number of Type-0 to PP0 variations needed.

CHAPTER VII

Conclusion

The Standard Model (SM) of Particle Physics was completed with the discovery of the Higgs boson in 2012. While the SM has had unprecedented success at describing the universe at a subatomic scale, it does not explain every natural phenomenon, such as dark matter. These shortcomings show that the SM is not the complete theory. Many extensions to the SM have been proposed, and a common feature in many of these extensions is the existence of a new type of particle called vector-like quarks (VLQs). This thesis presented two of the latest searches for VLQs using the full Run 2 dataset of 13 TeV pp-collisions produced by the LHC and recorded by the ATLAS detector.

The particles from the pp-collisions travel through the ATLAS detector, leaving signals in the detector subsystems. Algorithms take these signals and reconstruct physics objects for the physics analyses to use. Each physics object has a calibration to correct for any detector effects on the measurement of the kinematics of the object. A common object used in analyses is large-R jets. This thesis presented the work in calculating a calibration to the large-R jet energy measurement for high p_{T} jets.

The primary analysis presented in this thesis was a search for the pair production of VLQs decaying to SM W bosons and light quarks. This analysis improved the lower mass limit for these particles by a factor of two, representing the most stringent limits to date for such particles. Figure 43 shows the cross-section as a function of mass for VLQs decaying 100% to a W boson and light quark. VLQs with a mass below 1550 GeV are now excluded with a 95% confidence level.

The second analysis presented was a search for the pair production of VLQs decaying to SM W bosons and bottom quarks. This analysis is still blinded and not allowed to look at data within the signal regions. The expected lower mass limit was calculated, and the sensitivity is expected to be around 1550 GeV, a 200 GeV increase from the previous run of the analysis.

The LHC and the ATLAS will undergo an upgrade starting in 2026. One main upgrade for the ATLAS detector is the Inner Detector being upgraded to the all-silicon Inner Tracker (ITk). The final work presented in this thesis was designing prototype PCBs for the readout system of pixel modules in the ITk pixel detector.

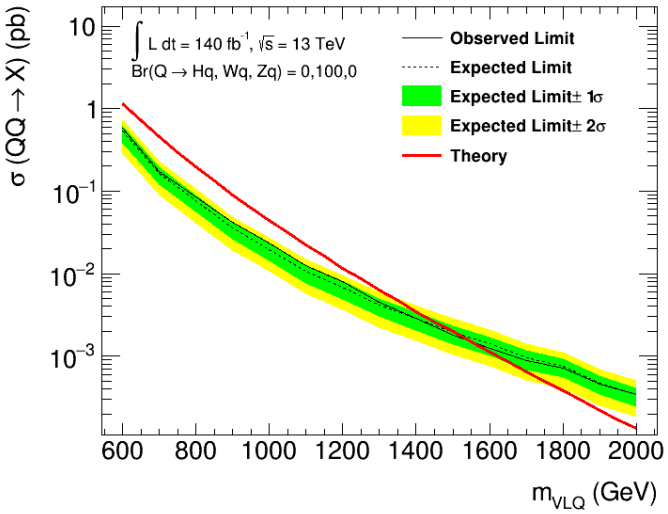

Figure 43: Cross-section upper limit vs. mass of the VLQ decaying 100% of the time to a W boson and light quark.

REFERENCES

[1] M Aaboud, Georges Aad, Brad Abbott, B Abeloos, SH Abidi, OS AbouZeid, NL Abraham, H Abramowicz, H Abreu, R Abreu, et al., *Search for pair production of heavy vector-like quarks decaying to high-p tw bosons and b quarks in the lepton-plus-jets final state in pp collisions at $\sqrt{s}$ = 13 tev with the atlas detector*, Journal of high energy physics **2017** (2017), no. 10, 1–40.

[2] Morad Aaboud, G Aad, B Abbott, J Abdallah, O Abdinov, B Abeloos, SH Abidi, OS AbouZeid, NL Abraham, H Abramowicz, et al., *Jet reconstruction and performance using particle flow with the atlas detector*, The European Physical Journal C **77** (2017), 1–47.

[3] Morad Aaboud, Georges Aad, Brad Abbott, B Abeloos, DK Abhayasinghe, SH Abidi, OS AbouZeid, NL Abraham, H Abramowicz, H Abreu, et al., *Search for single production of vector-like quarks decaying into wb in pp collisions at $\sqrt{s}$ = 13 tev with the atlas detector*, Journal of High Energy Physics **2019** (2019), no. 5, 1–56.

[4] Morad Aaboud, Georges Aad, Brad Abbott, B Abeloos, SH Abidi, OS AbouZeid, NL Abraham, H Abramowicz, H Abreu, R Abreu, et al., *Search for pair production of vector-like top quarks in events with one lepton, jets, and missing transverse momentum in $\sqrt{s}$ = 13 tev pp collisions with the atlas detector*, Journal of High Energy Physics **2017** (2017), no. 8, 1–40.

[5] Morad Aaboud, Georges Aad, Brad Abbott, B Abeloos, SH Abidi, OS AbouZeid, NL Abraham, H Abramowicz, H Abreu, Y Abulaiti, et al., *Search for pair production of up-type vector-like quarks and for four-top-quark events in final states with multiple b-jets with the atlas detector*, Journal of high energy physics **2018** (2018), no. 7, 1–68.

[6] Georges Aad, Tatevik Abajyan, B Abbott, J Abdallah, S Abdel Khalek, Ahmed Ali Abdelalim, R Aben, B Abi, M Abolins, OS AbouZeid, et al., *Observation of a new particle in the search for the standard model higgs boson with the atlas detector at the lhc*, Physics Letters B **716** (2012), no. 1, 1–29.

[7] Georges Aad, Tatevik Abajyan, Brad Abbott, Jalal Abdallah, S Abdel Khalek, Rosemarie Aben, B Abi, M Abolins, OS AbouZeid, H Abramowicz, et al., *Measurements of higgs boson production and couplings in diboson final states with the atlas detector at the lhc*, Physics Letters B **726** (2013), no. 1-3, 88–119.

[8] Georges Aad, B Abbott, J Abdallah, R Aben, M Abolins, OS AbouZeid, H Abramowicz, H Abreu, R Abreu, Y Abulaiti, et al., *Search for pair production of a new heavy quark that decays into a w boson and a light quark in p p collisions at s= 8 tev with the atlas detector*, Physical Review D **92** (2015), no. 11, 112007.

[9] Georges Aad, Brad Abbott, Dale Charles Abbott, L Ambroz, G Artoni, M Backes, WK Balunas, AJ Barr, L Beresford, D Bortoletto, et al., *Atlas data quality operations and performance for 2015–2018 data-taking*, Journal of instrumentation **15** (2020), no. 04.

[10] Georges Aad, JM Butterworth, J Thion, U Bratzler, PN Ratoff, RB Nickerson, JM Seixas, I Grabowska-Bold, F Meisel, S Lokwitz, et al., *The atlas experiment at the cern large hadron collider*, Jinst **3** (2008), S08003.

[11] Kenneth Aamodt, A Abrahantes Quintana, R Achenbach, S Acounis, D Adamová, C Adler, M Aggarwal, F Agnese, G Aglieri Rinella, Z Ahammed, et al., *The alice experiment at the cern lhc*, Journal of Instrumentation **3** (2008), no. 08, S08002.

[12] S. Agostinelli et al., *Geant4–a simulation toolkit*, Nucl. Instrum. Meth. A **506** (2003), 250–303.

[13] Juan Antonio Aguilar-Saavedra, Rachid Benbrik, Sven Heinemeyer, and Manuel Pérez-Victoria, *Handbook of vectorlike quarks: Mixing and single production*, Physical Review D **88** (2013), no. 9, 094010.

[14] A Augusto Alves Jr, LM Andrade Filho, AF Barbosa, I Bediaga, G Cernicchiaro, G Guerrer, HP Lima Jr, AA Machado, J Magnin, F Marujo, et al., *The lhcb detector at the lhc*, Journal of instrumentation **3** (2008), no. 08, S08005.

[15] Giorgio Apollinari, I Béjar Alonso, O Brüning, P Fessia, M Lamont, L Rossi, and L Tavian, *High-luminosity large hadron collider (hl-lhc). technical design report v. 0.1*, Tech. report, Fermi National Accelerator Lab.(FNAL), Batavia, IL (United States), 2017.

[16] Nima Arkani-Hamed, Andrew G Cohen, Emanuel Katz, and Ann E Nelson, *The littlest higgs*, Journal of High Energy Physics **2002** (2002), no. 07, 034.

[17] Nima Arkani-Hamed, Savas Dimopoulos, and Gia Dvali, *The hierarchy problem and new dimensions at a millimeter*, Physics Letters B **429** (1998), no. 3-4, 263–272.

[18] ATLAS Collaboration atlas. publications@ cern. ch, G Aad, Brad Abbott, Dale Charles Abbott, A Abed Abud, Kira Abeling, Deshan Kavishka Abhayasinghe, Syed Haider Abidi, OS AbouZeid, Nicola Louise Abraham, et al., *Muon reconstruction and identification efficiency in atlas using the full run 2 pp collision data set at s= 13 tev*, The European Physical Journal C **81** (2021), no. 7, 578.

[19] E. Boltezar, H. Haseroth, W. Pirkl, G. Plass, T. R. Sherwood, U. Tallgren, P. Tetu, D. Warner, and M. Weiss, *Performance of the new cern 50 mev linac*, IEEE Transactions on Nuclear Science **26** (1979), no. 3, 3674–3676.

[20] O Brüning, P Collier, S Lebrun, R Myers, J Poole, and P Proudlock, *Lhc design report, volume i, the lhc main ring*, CERN, Geneva (2004).

[21] M Capeans, T Flick, R Vuillermet, G Darbo, H Pernegger, K Einsweiller, M Garcia-Sciveres, M Elsing, O Rohne, and C Gemme, *Atlas insertable b-layer technical design report*, Tech. report, ATLAS-TDR-019, 2010.

[22] Shreyashi Chakdar, Kirtiman Ghosh, S Nandi, and Santosh Kumar Rai, *Collider signatures of mirror fermions in the framework of a left-right mirror model*, Physical Review D **88** (2013), no. 9, 095005.

[23] Serguei Chatrchyan, Vardan Khachatryan, Albert M Sirunyan, Armen Tumasyan, Wolfgang Adam, Ernest Aguilo, Thomas Bergauer, M Dragicevic, J Erö, C Fabjan, et al., *Observation of a new boson at a mass of 125 gev with the cms experiment at the lhc*, Physics Letters B **716** (2012), no. 1, 30–61.

[24] ATLAS Collaboration, *Search for pair production of vector-like quarks decaying to a w boson and light quark using 140 fb^{-1} of run 2 data from the atlas experiment*, (In Preparation).

[25] ———, *Search for pair-production of vector-like quarks in final states with one lepton, missing transverse momentum, and at least one b-jet using 140fb^{-1} of run 2 data from the atlas experiment*, (In Preparation).

[26] ATLAS collaboration et al., *Electron and photon reconstruction and performance in atlas using a dynamical, topological cell clustering-based approach*, Tech. report, LHC/ATLAS Experiment, 2017.

[27] Atlas Collaboration et al., *Performance of the atlas transition radiation tracker in run 1 of the lhc: tracker properties*, Journal of instrumentation **12** (2017), P05002.

[28] ———, *Atlas b-jet identification performance and efficiency measurement with $t\bar{t}$ events in pp collisions at $\sqrt{s}$= 13 tev*, arXiv preprint arXiv:1907.05120 (2019).

[29] ATLAS Collaboration et al., *Atlas flavour-tagging algorithms for the lhc run 2pp collision dataset*, arXiv preprint arXiv:2211.16345 (2022).

[30] CMS Collaboration, S Chatrchyan, G Hmayakyan, V Khachatryan, AM Sirunyan, W Adam, T Bauer, T Bergauer, H Bergauer, M Dragicevic, et al., *The cms experiment at the cern lhc*, Jinst **3** (2008), S08004.

[31] Roberto Contino, Yasunori Nomura, and Alex Pomarol, *Higgs as a holographic pseudo-goldstone boson*, Nuclear Physics B **671** (2003), 148–174.

[32] Thijs Cornelissen, M Elsing, W Liebig, S Fleischmann, and E Moyse, *Concepts, design and implementation of the atlas new tracking (newt)*, Tech. report, 2007.

[33] Abdelhak Djouadi and Alexander Lenz, *Sealing the fate of a fourth generation of fermions*, Physics Letters B **715** (2012), no. 4-5, 310–314.

[34] ATLAS Experiment, *Explore the atlas schematics*, https://atlas.cern/Resources/Schematics.

[35] Simone Gilardoni, Django Manglunki, Jean-Paul Burnet, Christian Carli, Michel Chanel, Roland Garoby, Massimo Giovannozzi, Steven Hancock, Helmut Haseroth, Kurt Hübner, et al., *Fifty years of the cern proton synchrotron: Volume 2*, arXiv preprint arXiv:1309.6923 (2013).

[36] Werner Herr and Bruno Muratori, *Concept of luminosity*, (2006).

[37] Roland Jansky, ATLAS Collaboration, et al., *The atlas fast monte carlo production chain project*, Journal of Physics: Conference Series, vol. 664, IOP Publishing, 2015, p. 072024.

[38] Steven Schramm, *Atlas jet reconstruction, calibration, and tagging of lorentz-boosted objects*, EPJ Web of Conferences, vol. 182, EDP Sciences, 2018, p. 02113.

[39] Saleh Sultansoy and Gokhan Unel, *The e6 inspired isosinglet quark and the higgs boson*, Physics Letters B **669** (2008), no. 1, 39–45.

[40] Wikipedia, *Standard model*, https://en.wikipedia.org/wiki/Standard_Model.